



ENGINEERING-PDH.com
ONLINE CONTINUING EDUCATION

SPACE WEATHER EMP BENCHMARKS

Main Category:	Environmental Engineering
Sub Category:	-
Course #:	ENV-125
Course Content:	49 pgs
PDH/CE Hours:	3

OFFICIAL COURSE/EXAM (SEE INSTRUCTIONS ON NEXT PAGE)

WWW.ENGINEERING-PDH.COM

TOLL FREE (US & CA): 1-833-ENGR-PDH (1-833-364-7734)

SUPPORT@ENGINEERING-PDH.COM

ENV-125 EXAM PREVIEW

- TAKE EXAM! -

Instructions:

- At your convenience and own pace, review the course material below. When ready, click “Take Exam!” above to complete the live graded exam. (Note it may take a few seconds for the link to pull up the exam.) You will be able to re-take the exam as many times as needed to pass.
- Upon a satisfactory completion of the course exam, which is a score of 70% or better, you will be provided with your course completion certificate. Be sure to download and print your certificates to keep for your records.

Exam Preview:

1. According to the reference material, Fluence is the rate at which particles flow through a unit area, given in units of particles/(cm²/s)
 - a. True
 - b. False
2. According to the reference material, what is the median 1-in-100-year benchmark for geo-electric exceedance amplitude among surveyed sites?
 - a. 0.32 V/km
 - b. 4.57 V/km
 - c. 0.26 V/km
 - d. 1.26 V/km
3. According to the reference material, what frequency range, in megahertz, does Global Positioning Systems (GPS) operate between?
 - a. 300-3,000
 - b. 1,176-1,602
 - c. 2,800
 - d. 4,000-20,000
4. Table 2 lists three types of ionizing radiation, their sources, and the hazards they pose. According to this table, which type of ionizing radiation has “Greatest hazard is > 30 MeV protons that can penetrate space suits & spacecraft walls.”
 - a. Solar energetic particles
 - b. Cosmic rays
 - c. Radiation belts - outer belts
 - d. Radiation belts - inner belts

5. Table 8 lists the Effect of extreme events on the ionosphere. Using this chart, which Geomagnetic Storm even occurs in the high and mid latitudes with the environmental effect of patches, plasma structures, and ionospheric gradients refract radio waves?
 - a. Polar Cap and Aurora
 - b. Traveling Ionospheric Disturbances
 - c. Equatorial Scintillation
 - d. Lateral Scintillation
6. The ionosphere can become turbulent due to small-scale irregularities that alter the amplitude and phase of transmitted signals. The term ionospheric scintillation is often used to describe this phenomenon.
 - a. True
 - b. False
7. According to the reference material, Solar radio bursts are emitted from the Sun during solar flares; on average, solar flares occur every 3.5 days at solar maximum and every ___ days at solar minimum.
 - a. 12
 - b. 15.5
 - c. 18.5
 - d. 20
8. According to the reference material, different layers in the ionosphere are labeled the H, J, and K regions as defined by the relative altitude above Earth's surface. These layers transmit, absorb, reflect, and refract radio signals depending on the density of the layer and frequency of the radio wave.
 - a. True
 - b. False
9. According to the reference material, at 400 kilometers, the thermosphere at mean levels of solar activity is dominated by atomic oxygen (O). At 250 kilometers molecular nitrogen (N₂) contributes a significant fraction, and at 850 kilometers _____ begins to dominate.
 - a. CO₂
 - b. Methane
 - c. Hydrogen
 - d. Helium
10. According to the reference material, Over the past 68 years, the daily F10.7 at 1 AU exceeded 300 solar flux units (sfu) on only 80 days in the upper atmospheric expansion.
 - a. True
 - b. False

Table of Contents

Introduction	1
Summary of Benchmarks.....	3
Benchmarks for Induced Geo-electric Fields	9
Benchmarks for Ionizing Radiation	12
Benchmarks for Ionospheric Disturbances.....	23
Benchmarks for Solar Radio Bursts.....	30
Benchmarks for Upper Atmosphere Expansion.....	34
Bibliography	43
Abbreviations	46

Introduction

The 2017 National Security Strategy¹ calls for the promotion of American resilience and space commerce, and for the U.S. to maintain the lead in space exploration. Space weather, a natural source of electromagnetic pulse (EMP), can disrupt, degrade, or damage infrastructure and technology systems, including the electrical power grid. For example, in 1989, a space weather event caused a blackout in Quebec that affected more than six million customers. Space weather can blackout air traffic control and high-frequency communications systems. Beyond terrestrial systems, space weather can affect satellite systems, interfere with GPS service, endanger the lives of humans in space, and delay the launch of space missions. This makes preparing for space weather events critical to national security, infrastructure services, space missions, and technology innovations (such as autonomous vehicles) that rely on communications systems and GPS for positioning, navigation, and timing services.

Recent executive actions identify priorities that necessitate the need to further prepare the Nation for effects of space weather phenomena, including EMP. Efforts to address the threat of space weather through enhanced research, operations, and mitigation activities can be leveraged to help address the threat of adversarial EMP. Benchmarks for space weather will enhance awareness of threats among critical infrastructure owners and operators in the private sector, and will serve as an input for academic and private sector innovation towards building a space weather- and EMP-ready Nation.

In accordance with these priorities and the existing policy on enhancing resilience to space weather, this report identifies initial benchmarks for five phenomena associated with space weather events:

1. Induced geo-electric fields
2. Ionizing radiation
3. Ionospheric disturbances
4. Solar radio bursts
5. Upper atmospheric expansion

The benchmarks are designed to capture an event's ability to affect the Nation, and provide clear and consistent descriptions of space weather events based on current scientific understanding and the historical record. The purpose of the benchmarks is to provide input for creating engineering standards, developing vulnerability assessments and risk estimates, establishing decision points and thresholds for action, understanding risk, developing more effective mitigation procedures and practices, and enhancing response and recovery planning. Their purpose is not to categorize or classify a space weather event's degree of impact on a technology system.

For each of the five phenomena, this report identifies benchmark values for two different scales: those that are likely to occur once in 100 years and those associated with the theoretical maximum. Each of the benchmarks specifies the physical characteristics and conditions against which a space weather event can be measured. The benchmarks describe the nature and intensity of extreme space weather events, providing a point of reference from which to improve understanding of the effects of space weather.

¹ Executive Office of the President, *National Security Strategy of the United States of America*, December 2017, <https://www.whitehouse.gov/wp-content/uploads/2017/12/NSS-Final-12-18-2017-0905.pdf>

For each benchmark, critical assumptions are described with their associated uncertainties. The benchmarks presented in this report are at different levels of maturity based on the current scientific understanding and available data. Where provided, benchmarks seek to supply parameters that are most useful to the relevant audience.

The Action Plan identifies a two-phase approach with different timelines to balance immediate needs for benchmarks with requirements for scientifically and statistically rigorous benchmarks. For Phase 1, the results of which are captured in this report, working groups associated with the SWORM Subcommittee conducted a quick-turnaround analysis to develop benchmarks using existing data sets and studies, where available. This report is informed by public feedback received from the Federal Register Notice and request for comment on a January 2017 draft of the Phase 1 benchmarks.²

For Phase 2, the Subcommittee will more rigorously analyze cases where a quick-turnaround analysis did not yield benchmarks of sufficient precision for their intended uses. In addition, the approach for Phase 2 will also be informed by public feedback received on the draft of the Phase 1 benchmarks. The Action Plan³ states that all benchmarks will be re-examined at least once every 5 years or when significant new data or models become available.

² Department of Commerce (DOC), “Notice of Availability of and Request for Public Comment on SPACE WEATHER EMP BENCHMARKS,” National Oceanic and Atmospheric Administration (NOAA), Federal Register 82, no. 13 (January 23, 2017): 7801–7802.

³ NSTC, SWORM Subcommittee, National Space Weather Action Plan, October 2015, https://www.sworm.gov/publications/2015/swap_final__20151028.pdf

Summary of Benchmarks

Table 1. Phase 1 benchmarks, parameters, and methods

Benchmarks for Induced Geo-Electric Fields	
Environmental parameter	Intense magnetic storms may induce geo-electric fields of sufficient strength to drive quasi-direct currents in electric power grids, sometimes causing blackouts and damaging transformers.
Methodology for determining benchmarks	Benchmarking for induced geo-electric field amplitudes used two geophysical quantities: the surface impedance relationship between geomagnetic variation and the induced geo-electric field, as well as a measure of geomagnetic activity at Earth's surface. Surface impedance values are obtained by magnetotelluric surveys, which have been completed for about half of the continental United States. Surface geomagnetic activity is routinely measured at magnetic observatories and variometer stations, and geomagnetic variations during a once-per-century event are estimated by a statistical analysis.
1-in-100-year benchmarks	The median once-per-century geo-electric exceedance amplitude among surveyed sites (see Figure 1) is 0.26 volts per kilometer (V/km), with amplitudes exceeding 14 V/km in Minnesota. One standard-deviation error, the result of statistical variance in the geomagnetic data, is estimated to be about 30 percent, which is small compared to the site-to-site differences. The full benchmark of once-per-century geo-electric amplitudes across the United States, where data is available, is displayed in Figure 1.
Theoretical maximum benchmarks	Not feasible to compute benchmarks. Higher frequency amplitudes cannot be reasonably estimated from the observatory data, and while lower frequency harmonics generally yield smaller geo-electric amplitudes, additional investigation would help inform this issue.
Benchmarks for Ionizing Radiation	
Environmental parameter	Solar energetic particle (SEP) events, galactic cosmic rays (GCRs), and radiation belts around Earth can interact in complicated ways to augment the flux and fluence of protons, electrons, and other particles near Earth.
Methodology for determining benchmarks	<p>Statistical information on the probability versus intensity of fluxes or fluences from spacecraft were used to set benchmarks for solar particle events and the radiation belts. Estimates of the probability and severity of extreme flux events were obtained using extreme value theory (EVT), which is aimed at characterizing the low-frequency/high-severity tail of the probability distribution.</p> <p>Approximations of variations in galactic cosmic rays (GCRs) caused by total solar wind and magnetic field intensity in the heliosphere were used to benchmark GCR ionizing radiation. As a theoretical maximum, the GCR fluence is equal to that of the local interstellar spectra (LIS), essentially assuming that there is no solar modulation (i.e. that the heliopause has moved inside 1 AU)</p>

Benchmarks for Ionizing Radiation (continued)

1-in-100-year benchmarks

Benchmarks for SEP events, GCRs, and electron radiation belts (at selected locations) are provided below. For more benchmarks, see the full chapter on Ionizing Radiation.

Differential GCR Flux (particles/(cm ² sr s MeV/n)) at 1 AU, $\phi^a = 200$ MV			
Uncertainties are 10%-25%			
Energy/nucleon	Hydrogen	Oxygen	Iron
10 MeV	1.3×10^{-4}	5.3×10^{-7}	1.2×10^{-7}
100 MeV	5.3×10^{-4}	1.5×10^{-6}	2.9×10^{-7}
1 GeV	1.2×10^{-4}	2.4×10^{-7}	3.7×10^{-8}
100 GeV	1.2×10^{-6}	2.1×10^{-9}	3.9×10^{-10}
1000 GeV	2.9×10^{-9}	5.0×10^{-12}	1.2×10^{-12}

Electron Radiation Belt Flux		
Location	Energy	Differential Flux (cm ⁻² s ⁻¹ sr ⁻¹ MeV ⁻¹)
INTEGRAL/IREM at L*=6.0	2.05 MeV	1.58×10^5
	1.82 MeV	1.76×10^5
	1.27 MeV	5.99×10^5
	690 keV	4.68×10^6
INTEGRAL/IREM at L*=4.5	2.05 MeV	5.79×10^5
	1.82 MeV	7.29×10^5
	1.27 MeV	2.52×10^6
	690 keV	1.46×10^7

Proton Radiation Belt Flux		
Energy (MeV)	1-in-100-Year Flux (protons/(cm ² s MeV)) based on Gumbel ^b Fit	Estimate of Uncertainty (ratio of exponential and Gumbel ^b fit)
1	2.53×10^{10}	~ 2
3	1.97×10^{10}	~ 25
5	1.23×10^8	~ 2
10	4.49×10^{10}	~ 20

Benchmarks for Ionizing Radiation (continued)			
Theoretical maximum benchmarks	Differential GCR Flux (particles/(cm ² sr s MeV/n)) at 1 AU, $\phi^a = 0$ MV		
	Uncertainties are 10%-25%		
	Energy/nucleon	Hydrogen	Oxygen
	10 MeV	2.6×10^{-1}	6.8×10^{-5}
	100 MeV	9.4×10^{-3}	6.8×10^{-5}
	1 GeV	2.2×10^{-4}	3.2×10^{-7}
	100 GeV	1.3×10^{-6}	2.2×10^{-9}
	1000 GeV	2.9×10^{-9}	5.1×10^{-12}
Statistical maximum benchmarks	Integral SEP Fluence (protons/cm ²) at Geostationary Orbit (GEO) ^c		
	Energy (MeV)	Upper Limit	Maximum value with uncertainty (Upper Limit +1 sigma)
	1	1.56×10^{11}	3.54×10^{11}
	10	3.49×10^{10}	7.93×10^{10}
	100	1.45×10^9	3.30×10^9
	500	2.21×10^7	5.01×10^7
	Electron Radiation Belt Flux		
	Location	Energy	Differential Flux (cm ⁻² s ⁻¹ sr ⁻¹ MeV ⁻¹)
	GEO (LANL)	2.65 MeV	$5.9 [4.7, 7.3] \times 10^4$
		625 keV	$4.1 [3.2, 5.2] \times 10^6$
		270 keV	$2.0 [1.5, 2.6] \times 10^7$
	INTEGRAL/IREM at L*=6.0	1.82 MeV	1.98×10^5
		1.27 MeV	8.11×10^5
		690 keV	4.82×10^6
INTEGRAL/IREM at L*=4.5	2.05 MeV	6.08×10^5	
	1.82 MeV	8.10×10^5	
	1.27 MeV	4.74×10^6	
	690 keV	1.51×10^7	

Benchmarks for Ionospheric Disturbances				
Environmental parameter	The ionosphere is highly variable and is driven externally by solar extreme ultraviolet (EUV) and X-ray irradiance, geomagnetic storms, and the neutral atmosphere. These drivers can affect the total electron content (TEC), highest affected frequency (HAF), maximum usable frequency (MUF), height of the F ₂ layer (hmF ₂), peak density of the F ₂ layer (NmF ₂), and the phase and amplitude scintillation indices Sigma-Phi and S4. Ionospheric variability affects radio signal propagation by changing the reflection, refraction, absorption, and delay of the radio signal.			
Methodology for determining benchmarks	The extreme impacts of ionospheric disturbances on communication, navigation, and positioning systems would be fully described by global maps of a number of parameters, including the TEC, HAF, MUF, hmF ₂ , NmF ₂ , and the phase and amplitude scintillation indices Sigma-Phi and S4.			
1-in-100-year benchmarks	Not feasible to compute benchmark. Complexities in modeling ionospheric disturbances prevented setting useful benchmarks with reasonable uncertainty.			
Theoretical maximum benchmarks	<p>Not feasible to compute benchmarks. Advances in scientific understanding of the entire magnetosphere-ionosphere-thermosphere (MIT) system and its response to extreme geomagnetic storms would improve the ability to quantify benchmarks for ionospheric disturbances.</p> <p>While benchmarks were not developed, values were measured during the intense 2003 Halloween event for ionospheric disturbances. These include a vertical TEC of 250 TECu (where 1 TECu = 1 × 10¹⁶ electrons m⁻²) with an associated error of approximately 3 TECu, a TEC spatial range gradient of 40 cm/km, and a TEC temporal range gradient of 15 cm/s.^{d, e, f} These conditions could last up to several days.^g</p>			
Benchmarks for Solar Radio Bursts				
Environmental parameter	Solar radio bursts are emitted from the Sun during solar flares; on average, solar flares occur every 3.5 days at solar maximum and every 18.5 days at solar minimum. Solar flux units (sfu) are used to describe the intensity of the incident solar flare at Earth.			
Methodology for determining benchmarks	The 1-in-100-year benchmarks were defined using the peak flux distribution of solar radio bursts for the frequency bands that align with standard usage, as presented by Nita et al. ^h The authors' analysis relies on the most extensive data set on solar radio bursts, collected by the United States Air Force's Radio Solar Telescope Network (RSTN), with data from 1960 to present.			
1-in-100-year benchmarks	Frequency Band Name	Frequency (megahertz)	Benchmark (sfu) ⁱ	Error Bars (sfu) ⁱ
	Very High Frequency (VHF)	30–300	2.8 × 10 ⁹	[-2.5 × 10 ⁹ , +0]
	Ultra High Frequency (UHF)	300–3000	1.2 × 10 ⁷	[-1 × 10 ⁷ , +0]
	Global Positioning System (GPS)	1,176–1,602	1.2 × 10 ⁷	[-1 × 10 ⁷ , +0]
	F _{10.7}	2,800	1.3 × 10 ⁷	[-1 × 10 ⁷ , +0]
	Microwave	4,000–20,000	3.7 × 10 ⁷	[-3 × 10 ⁷ , +0]
Theoretical maximum benchmarks	Not feasible to compute benchmarks. Identifying the theoretical maximum intensity from solar radio bursts in each frequency band could be informed by determining the maximum feasible brightness temperature and area of the burst source.			

Benchmarks for Upper Atmosphere Expansion				
Environmental parameter	Upper atmosphere expansion refers to changes in the thermosphere that can affect satellite drag at low Earth-orbit (LEO). The primary expansion effect arises from an increase in temperature, which can be driven by solar or geomagnetic activity, which causes an increase in neutral density at a fixed altitude in Earth's upper atmosphere. This heating can be driven by solar or geomagnetic activity. This is quantified by the percent neutral density increase.			
Methodology for determining benchmarks	<p>The benchmark from solar extreme ultraviolet (EUV) and far ultraviolet (FUV) radiation on timescales greater than one day was determined using the NRLMSISE-00 empirical neutral density model.^j The neutral density response is defined at 250 kilometers, 400 kilometers, and 850 kilometers altitude as percent increases relative to empirical model reference values using 240 and 200 solar flux units (sfu) for the F10.7 daily and 81-day mean, respectively.</p> <p>The benchmark from the impact of EUV enhancement during impulsive events, such as solar flares, estimates a 100-year flare as an X30 and a theoretical maximum as an X40.^k The values quoted are peak dayside neutral density increases relative to the background before the flare. The values are quoted at 400 kilometers altitude only and are the response at a median F10.7 solar flux level of 150 sfu.</p> <p>The benchmark from the impact of coronal mass ejections (CMEs) uses the predicted 1-in-100-year solar wind values to drive the Weimer empirical magnetospheric convection model with expected magnetospheric saturation. The percent increase is relative to the values experienced during the Halloween or Bastille Day storms as predicted by the CTIPe physical model.</p>			
1-in-100-year benchmarks	Cause of Upper Atmosphere Expansion	Altitude (km)	Benchmark (percent neutral density increase) ^m	Associated Uncertainty
	Solar Extreme Ultraviolet and Far Ultraviolet Radiation	250	50%	± 30%
		400	100%	± 30%
		850	200%	± 30%
	Solar EUV Radiation Enhancement during Solar Flares	400	75%	factor of 2
Coronal Mass Ejections Driving Geomagnetic Storms	400	400%	± 100%	
Theoretical maximum benchmarks	Solar Extreme Ultraviolet and Far Ultraviolet Radiation	250	100%	factor of 2
		400	160%	factor of 2
		850	300%	factor of 2
	Solar EUV Radiation Enhancement during Solar Flares	400	135%	factor of 2
	Coronal Mass Ejections Driving Geomagnetic Storms	400	Not feasible to compute benchmarks	± 100%

Notes: INTEGRAL/IREM is the Radiation Environment Monitor (IREM) on board the International Gamma Ray Astrophysical Laboratory (INTEGRAL) spacecraft, which is in an elliptical orbit with perigee of 9,000 km and apogee of 155,000 km. $L^* = n$ describes a set of planetary magnetic field lines which cross the Earth's magnetic equator at n earth radii from the center of the Earth, e.g., $L^* = 6$ describes the set of magnetic field lines three earth radii from the center.

- ^a ϕ is the modulation parameter used in the force-field modulation approximation.
- ^b The Gumbel function is a particular case of the generalized extreme value distribution function.
- ^c Integrated over all energies greater than the nucleon energy of interest
- ^d A. J. Mannucci, "Global Ionospheric Storms," white paper submitted to the Space Studies Board of the U.S. National Research Council for its 2010 "decadal survey" in solar and space physics (heliophysics), 2010.
- ^e P. Stephens et al., "New leveling and bias estimation algorithms for processing COSMIC/FORMOSAT-3 data for slant total electron content measurements," *Radio Science* 46 (2011): RS0D10. doi: 10.1029/2010RS004588
- ^f S. Datta-Barua, "Ionospheric Threats to Space-Based Augmentation System Development," presented at the Proceedings of the 17th International Technical Meeting of the Satellite Division of The Institute of Navigation (ION GNSS 2004), Long Beach, California, 2004.
- ^g M. Hapgood et al., *Summary of Space Weather Worst-Case Environments*, RAL technical report, Revised edition, RAL-TR-2016-006, May 2016.
- ^h G. M. Nita et al. "The Peak Flux Distribution of Solar Radio Bursts." *Astrophysical Journal* 570 (May 2002): 423–438.
- ⁱ Solar flux is measured in watts (W) per square meter (m^2) per hertz (Hz), with 1 sfu equal to $10^{-22} \text{ W m}^{-2} \text{ Hz}^{-1}$.
- ^j J. M. Picone et al., "NRLMSISE-00 Empirical Model of the Atmosphere: Statistical Comparisons and Scientific Issues," *Journal of Geophysical Research* 107 (2002): A12, 1468; J. T. Emmert, "Thermospheric Mass Density: A Review," *Advances in Space Research* 56 (2015): 773–824.
- ^k C. J. Schrijver et al. "Estimating the Frequency of Extremely Energetic Solar Events, Based on Solar, Stellar, Lunar, and Terrestrial Records." *Journal of Geophysical Research* 117 (2012): A08103, based on an NRC study.
- ^l D. R. Weimer, "Improved Ionospheric Electrodynamics Models and Application to Calculating Joule Heating Rates," *Journal of Geophysical Research* 110 (2005): A05306.
- ^m See methodology description above for details on benchmarked values for each cause of upper atmosphere expansion.

Benchmarks for Induced Geo-electric Fields

1. Space Weather Action Plan 1.1.1

Action 1.1.1 of the Space Weather Action Plan states: “The Department of the Interior (DOI), the Department of Commerce (DOC), and the National Aeronautics and Space Administration (NASA), in coordination with the Department of Homeland Security (DHS), the Department of Energy (DOE), and the National Science Foundation (NSF), will: (1) assess the feasibility of establishing functional benchmarks [for induced geo-electric fields] using currently available storm data sets, existing models, and published literature; and (2) use the existing body of work to produce benchmarks [for induced geo-electric fields] for specific regions of the United States.”

2. Induced Geo-electric Fields

Geo-electric fields are induced in Earth’s electrically conducting interior by time-dependent geomagnetic field variation. During intense magnetic storms, induced geo-electric fields can drive quasi-direct currents of electricity of sufficient strength to interfere with operation of the power grid, sometimes causing blackouts and damaging transformers. Geomagnetic disturbances have affected power grids in the past. For example, in March 1989, an intense magnetic storm caused the collapse of the entire Hydro-Quebec power grid in Canada. More recently, in October 2003, a magnetic storm caused disturbances in power grids in Scotland and Sweden. According to some scenarios, the future occurrence of an extremely intense magnetic storm could result in widespread and possibly cascading failures if the power grid is not sufficiently resilient to the effects of space weather. Even for brief periods of time, loss of power can prove disruptive for communities.

3. Methodology for Establishing Benchmarks for Induced Geo-electric Fields

This task focused on the development of a formal statistical product in terms of maps of geo-electric hazard. For practical evaluation of geo-electric hazards, estimates of two geophysical quantities are needed: (1) the surface impedance relationship between geomagnetic variation and the induced geo-electric field and (2) a measure of geomagnetic activity realized at Earth’s surface.

Surface impedance is a function of the three-dimensional conductivity structure of the solid Earth and ocean. It is usually expressed in the Fourier-transformed frequency domain as a tensor. Impedance can differ greatly from one geographic location to another; it is not readily estimated from geological and tectonic models. Impedance is measured, however, during magnetotelluric surveys, such as the one sponsored by the NSF’s EarthScope program,⁴ which has, so far, been completed for about half of the contiguous United States.

Surface geomagnetic activity is measured at magnetic observatories, such as those operated within the INTERMAGNET consortium,⁵ or at variometer stations, such as those of the ULTIMA consortium.⁶ For purposes of hazard assessment, analysis of magnetometer time series can be focused on either the time-autocorrelated waveform nature of the data, or it can be focused on statistical analysis of

⁴ A. Schultz et al. “USArray TA Magnetotelluric Transfer Functions: REU60, 2006–2018,” doi:10.17611/DP/11455918. Retrieved from the IRIS database August 16, 2017.

⁵ J. J. Love and A. Chulliat, “An International Network of Magnetic Observatories,” *EOS, Transactions, American Geophysical Union* 94, no. 42 (2013): 373–384, doi:10.1002/2013EO42

⁶ K. Yumoto et al., “ULTIMA of Ground-Based Magnetometer Arrays for Monitoring Magnetospheric and Ionospheric Perturbations on a Global Scale,” presented at 2012 Fall Meeting, AGU, San Francisco, California.

characteristic features identified in the data. These two approaches are orthogonal, but knowing the results of both is useful. This report takes a statistical approach for benchmarking induced geo-electric field amplitudes that are unlikely to occur more than once in 100 years.

To use the measured impedances and to perform a statistical analysis of observatory data, Love et al. focused on sinusoidal variation over a finite window of time.⁷ Analysis of geomagnetic variation is limited on the high-frequency end of the spectrum by the one-minute sampling rate of the historical magnetic observatory data. For specificity, the amplitudes of geomagnetic activity Fourier waveforms having period of 240 seconds and persisting over a duration of 600 seconds were estimated from approximately 30 years of observatory data. This was done for both north-south (p_x) and east-west (p_y) magnetic vector components. These amplitudes were then extrapolated using a simple statistical model to once-per-hundred-year values. The frequency domain multiplication of a Fourier magnetic field amplitude with an impedance tensor gives a geo-electric amplitude.

4. Benchmarks

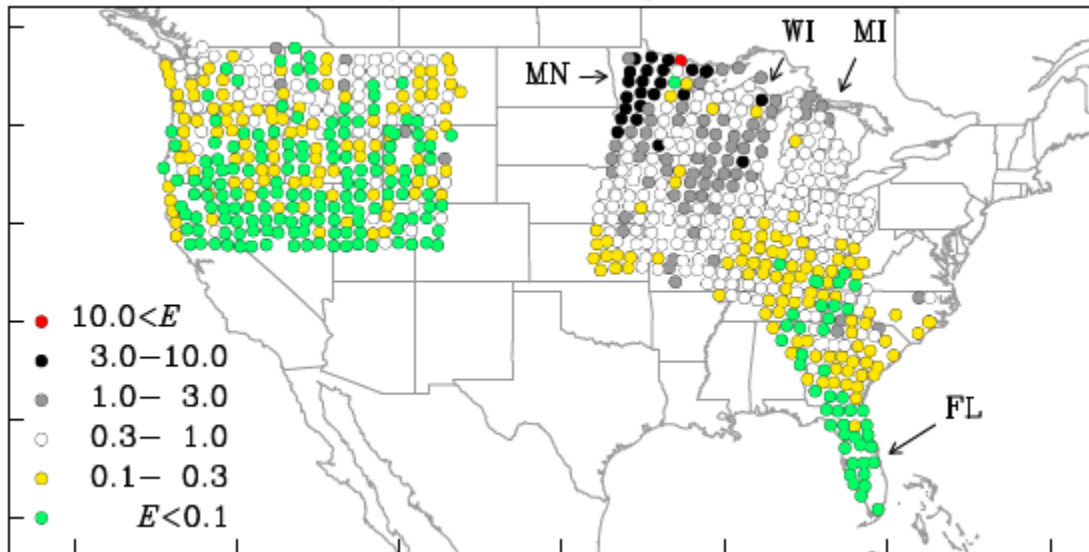
For the one-in-100-year benchmark, detailed results are discussed in Love et al.⁸ A map of once-per-century geo-electric exceedance amplitudes (E_e^x) for p_x is shown in Figure 1. Depending on location, once-per-century geo-electric exceedance amplitudes can exceed 1 volt per kilometer (V/km) in many places across the northern Midwest United States and some places in the Eastern United States. Among the surveyed sites, the median geo-electric amplitude is 0.26 V/km, but because of the combination of geographic differences in geomagnetic activity and Earth-surface impedance, geo-electric amplitudes differ by over two orders of magnitude. At some sites in Minnesota, for example, once-per-century amplitudes exceed 3.00 V/km. Across other areas, such as in Florida, these amplitudes are less than 0.1 V/km. In northern Minnesota, once-per-century amplitudes exceed 14.00 V/km, while just over 100 kilometers away, amplitudes are only 0.08 V/km. One standard-deviation error, the result of statistical variance in the geomagnetic data, is estimated to be about 30 percent, which is small compared to the differences.

At some sites in the northern Midwest United States, once-per-century geo-electric amplitudes exceed 2 V/km, which is the level inferred to have been realized in Quebec during the March 1989 storm. As a point of reference only, amplitudes in some regions of northern Minnesota exceed the once-per-century baseline amplitude of 8 V/km (without latitude corrections) used by the North American Electric Reliability Corporation (NERC) in its benchmark study using synthetic Earth impedances.⁹

⁷ J. J. Love et al., "Geoelectric Hazard Maps for the Continental United States," *Geophysical Research Letters*, 43, no. 18 (2016.): 9415–9424, doi:10.1002/2016GL070469

⁸ Ibid.

⁹ NERC, "Benchmark Geomagnetic Disturbance Event Description" (2014): 1–26.



Source: Love et al., “Goelectric Hazard Maps for the Continental United States,” *Geophysical Research Letters* 43 (18, 2016), 9415–9424, doi:10.1002/2016GL070469

Note: No estimates are available outside of survey sites shown.

Figure 1. Once-per-century geo-electric exceedance amplitudes¹⁰ (E in V/km), for north-south geomagnetic variation at 240 seconds (and over 600 seconds)

No theoretical maximum benchmarks were computed for the following reason: higher frequency amplitudes cannot be reasonably estimated from the observatory data; lower frequency harmonics, or those persisting for long periods of time, will generally yield smaller geo-electric amplitudes; additional investigation could inform understanding of the issue. Phase 2 activities will be directed toward (1) developing hazard maps for other frequencies, (2) developing scenario studies for individual magnetic storms (time-dependent maps of induced geo-electric fields), (3) investigating “coast effects” related to the conductivity contrast between the solid Earth and ocean, (4) developing a theoretical benchmark, and (5) assessing hazards at additional locations on the map, potentially including Canada.

¹⁰ Statistical values for 100 years are often reported as exceedances for all types of geophysical benchmarks. Specific values are usually not described in terms of statistics; what is described is a range of values, in this case 100-year “value” is a value that is exceeded, on average, once per 100 years.

Benchmarks for Ionizing Radiation

1. Space Weather Action Plan 1.2.1

Action 1.2.1 of the Space Weather Action Plan states: “NASA and DOC, in coordination with NSF, the Department of Transportation (DOT), the Department of Defense (DOD), and the Federal Communications Commission (FCC), will: (1) assess the feasibility and utility of establishing functional benchmarks for ionizing radiation using the existing models and body of literature for this phenomenon; and (2) use the existing body of work to produce benchmarks.”

2. Ionizing Radiation

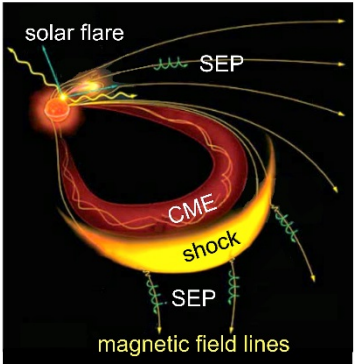
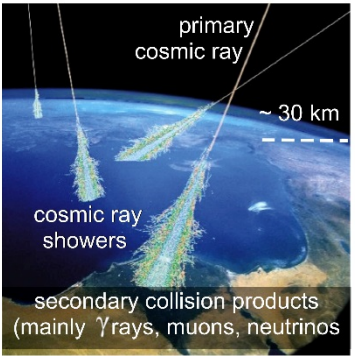
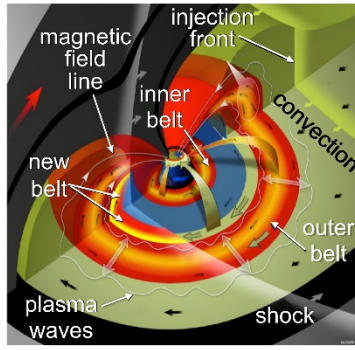
A major consideration in setting environmental benchmarks for ionizing radiation is to select the types of particles and energy ranges that have detrimental effects on vulnerable infrastructures and assets critical to the Nation’s economic and social well-being. The immediate need is to develop plans for coping with low-frequency/high-intensity space weather events, thus the focus on benchmarking worst-case and 1-in-100-year fluxes for each type of radiation at locations of interest. Worst-case fluxes for solar energetic particles and radiation belt populations are estimated with statistical maxima using observational data, because it is not feasible to calculate theoretical maxima, the maximum values these populations could possibly achieve, until a stronger theoretical foundation has been developed. However, a theoretical maximum for galactic cosmic rays is provided later in this chapter by assuming the flux distribution in the Local Interstellar Medium is not attenuated during transport to Earth.

Different types and energy ranges of ionizing radiation present hazards for satellites, astronauts, airline crews, and aviation communication. Exposure of satellites to enhanced fluxes of ionizing radiation can cause operational anomalies and damage to electronics, solar arrays, and optical systems. On the international space station this exposure presents a significant hazard to astronauts. The highest energy radiation penetrates deeply into the atmosphere and can be hazardous to airline crews on polar routes and significantly degrade high frequency (HF) communication via polar cap absorption events. Each of the specific species and energy ranges of ionizing radiation at key altitudes and locations responds differently to disruptions in the space environment. Environmental benchmarks for ionizing radiation must capture this complexity to maximize their future usefulness in designing around or mitigating hazards to vulnerable technologies, astronauts, and aviation crews during an extreme event.

Presented here is a set of benchmark values for only the most representative species, locations, and energy ranges along with explanatory material needed to understand how these extreme values were estimated. Due to the complexity and diversity of ionizing radiation hazards, the literature survey, undertaken to produce the Phase 1 benchmarks, captured more extensive information on the characteristics of each type of radiation and enabled a description of worst case and 1-in-100-year values on a finer energy resolution and covering more species of GCRs and SEPs.

A summary of the major types of radiation is given in Table 2.

Table 2. Three types of ionizing radiation, their sources, and the hazards they pose

<p>Solar Energetic Particles (SEPs)</p> 	<p>Type</p>	<p><u>Ions</u>: 1 mega-electron volt (MeV) to 20 giga-electron volt (GeV) hydrogen (H), helium (He), and heavy ions <u>Electrons</u>: Smaller fluxes with particle energies up to 10 MeV</p>
	<p>Source</p>	<p>Accelerated in flares, at shocks in the corona, and at interplanetary shocks, in particular those ahead of fast coronal mass ejections</p>
	<p>Hazard</p>	<p><u>Ions</u>: > 500 MeV: penetrate to ground level > 100 MeV: radiation hazard for airplane crews and passengers >30 MeV hazard for space tourism <u>Electrons</u> Penetrate into polar cap region. Reach the moon and the Lagrangian points where space missions reside.</p>
<p>Cosmic Rays</p> 	<p>Type</p>	<p>Near-constant isotropic flux. Nuclei of all natural elements in the Periodic Table: 90% H, 9% He, 1% heavier elements Energy Range: 1MeV–1 billion MeV</p>
	<p>Source</p>	<p>Not fully understood. Thought to originate in the large, expanding shells of supernovas. A small portion are accelerated at neutron stars or black holes.</p>
	<p>Hazard</p>	<p>Radiation hazard for astronauts and airplane crews. Effects of the primary cosmic rays scale with the square of the atomic number. Small percentages of heavy ions have large effects. Generate particle showers passing through thin mechanical shielding or the atmosphere. The atmosphere absorbs most of the cosmic ray energy before reaching the surface. However, protection from cosmic rays in space is the most difficult of all ionizing radiation.</p>
<p>Radiation Belts</p> 	<p>Type</p>	<p><u>Inner belt</u> (1.2-3 Earth radii): > 1 MeV H⁺ (proton), <MeV electrons <u>Outer belt</u> (3-10 Earth radii): 0.1–10 MeV electrons, < 1 MeV H⁺ (proton)</p>
	<p>Source</p>	<p>Intensity determined by the balance among radial diffusion, wave-particle interactions, non-adiabatic processes and (inner belt) neutrino decay. Outer electron belt drops out & reforms in response to space weather. New belts rapidly formed in response to interplanetary shocks/SEPs</p>
	<p>Hazard</p>	<p><u>Inner belt</u>: Greatest hazard is > 30 MeV protons that can penetrate space suits & spacecraft walls. An expanded inner belt may encompass the International Space Station and low Earth orbit (LEO) satellites. <u>Outer belt</u>: 0.1–10 MeV electrons cause surface charging, arcing & phantom commands on satellites</p>

3. Benchmarks for Ionizing Radiation

Solar Particle Events

Worst-case fluence is estimated by dividing the SEP energy spectra up into energy bins and performing a worst-case analyses for each bin using the methods of the Maximum Entropy Principle and Extreme Value Theory to construct an upper limit energy spectrum. The concepts behind Extreme Value Analysis are described in a later section on radiation belt benchmarks. As discussed by Xapsos et al. “A reasonable interpretation for the upper limit fluence parameter is that it is the best value that can be determined for the largest possible event fluence, given limited data. It is not an absolute upper limit but is a practical and objectively determined guideline for use in limiting design costs.”¹¹ This upper limit or statistical maximum spectra along with the +1 sigma estimate is given in Table 3.

Table 3. Integral SEP fluence for the statistical maximum case

SEP Integral Fluence (protons/cm ²) at Geostationary Orbit (GEO) ^a								
Energy (MeV/nucleon)	Upper Limit	Upper Limit + 1 Sigma	Energy (MeV/nucleon)	Upper Limit	Upper Limit + 1 Sigma	Energy (MeV/nucleon)	Upper Limit	Upper Limit + 1 Sigma
1	1.56×10^{11}	3.54×10^{11}	9	3.84×10^{10}	8.71×10^{10}	80	2.37×10^9	5.39×10^9
2	1.09×10^{11}	2.46×10^{11}	10	3.49×10^{10}	7.93×10^{10}	90	1.82×10^9	4.14×10^9
3.2	8.44×10^{10}	1.92×10^{11}	20	1.94×10^{10}	4.39×10^{10}	100	1.45×10^9	3.30×10^9
4	7.41×10^{10}	1.68×10^{11}	32	1.24×10^{10}	2.82×10^{10}	200	2.80×10^8	6.36×10^8
5	6.46×10^{10}	1.47×10^{11}	40	9.48×10^9	2.15×10^{10}	250	1.57×10^8	3.56×10^8
6.3	5.30×10^{10}	1.20×10^{11}	50	6.38×10^9	1.45×10^{10}	320	7.87×10^7	1.79×10^8
7.1	4.76×10^{10}	1.08×10^{11}	63	4.00×10^9	9.09×10^9	400	4.17×10^7	9.46×10^7
8	4.27×10^{10}	9.70×10^{10}	71	3.11×10^9	7.07×10^9	500	2.21×10^7	5.01×10^7

^a Integrated over all energies greater than the nucleon energy of interest

Note that fluence and flux units are both used to describe ionizing radiation in this chapter. Flux is the rate at which particles flow through a unit area, given in units of particles/(cm² s). Fluence is the time-integrated flux or the number of particles delivered to a unit area over some interval of time, given in units of particles/cm². This quantity does not contain information about the directionality of the flux. The differential flux contains directional information expressed as a function of solid angle and may also be expressed as a function of energy, given in units of particles/(cm² s sr) or particles/(cm² s sr keV), respectively.

¹¹ M. A. Xapsos et al., “Probability Model for Worst Case Solar Proton Event Fluences,” *IEEE Transactions on Nuclear Science* 46, no. 6 (December 1999): 1481–5, 1485.

Solar energetic particles with energies >100 MeV will penetrate down to the altitude of commercial polar flight routes (~30,000 feet or 10 kilometers) exposing airplane crew and passengers to increased radiation. SEP with energies above 30 MeV will increase radiation doses at the “edge” of space (100,000 feet or 30 kilometers) now accessed by space tourism aboard high altitude balloons.

Galactic Cosmic Rays (GCRs)

The primary variation in GCRs is due to the modulation stemming from the 11-year solar cycle¹², with a minimum of GCRs during the solar maximum, and a maximum during periods of low solar activity. The most recent solar minimum, with its exceptionally low levels of solar activity, led to the highest GCR fluxes observed in the space age (i.e., since the late 1950s).

The 1-in-100-year benchmarks for GCR fluxes shown in Table 4 were derived using local interstellar spectra (LIS) parameters from O’Neill, Golge, and Slaba, modulated with $\phi = 200$ megavolts (MV).¹³ Transport of GCRs through the heliosphere is a complicated problem, but a simple one-parameter “force-field approximation”¹⁴ can be used to benchmark GCR ionizing radiation. The modulation parameter (ϕ) in the force-field modulation approximation¹⁵ may be used to account for attenuation of the GCRs due to the state of the heliosphere. The ϕ is in units of rigidity (MV), and is proportional to the momentum/charge required for a particle to penetrate the heliosphere. Larger values of ϕ represent lower GCR fluxes reaching Earth. The value of ϕ can be approximated from solar activity indices, such as sunspot number, but a more accurate derivation can be obtained from current GCR data, such as those available from the Advanced Composition Explorer (ACE) spacecraft.

As a completely worst-case GCR intensity, one can take the local interstellar spectra (LIS), essentially assuming that there is no solar modulation or $\phi=0$ (i.e. that the heliopause has moved inside 1 AU) (Table 5). The LIS does change with time, but the time scales are tens of thousands of years or longer. Tables 4 and 5 give the most important elements, but GCRs composed of all the other elements will be present, and their fluxes can be calculated.

¹² The solar cycle refers to the periodic increase and decrease in solar activity caused by the reversal of the Sun’s magnetic poles. The solar cycle takes place over approximately 11 years and is tracked by counting the number of sunspots, an indicator of solar activity. For more information, see NASA’s primer on the solar cycle:

https://www.nasa.gov/mission_pages/sunearth/news/solarcycle-primer.html. Plots of the official count of daily and monthly sunspot numbers are available at the World Data Center - Sunspot Index and Long-term Solar Observations: <http://sidc.be/silso/datafiles#total>

¹³ P. M. O’Neill, S. Golge, and T. C. Slaba, “Badhwar-O’Neill 2014 Galactic Cosmic Ray Flux Model Description,” NASA/TP-2015-218569 (Houston, Texas: NASA Johnson Space Center, March 2015).

¹⁴ L. J. Gleeson and W. I. Axford, “Solar Modulation of Galactic Cosmic Rays,” *Astrophysical Journal* 154 (December 1968): 1011–26.

¹⁵ Gleeson and Axford. “Solar Modulation of Galactic Cosmic Rays.”

Table 4. Differential GCR fluxes for the most abundant elements at 1 astronomical unit (AU) for the 1-in-100-year case

Differential GCR Flux (particles/(cm² sr s MeV/n)) at 1 AU, $\phi = 200$ MV					
Uncertainties are 10%-25%					
Energy/nucleon	Hydrogen	Helium	Carbon	Oxygen	Iron
10 MeV	1.3×10^{-4}	1.7×10^{-5}	6.1×10^{-7}	5.3×10^{-7}	1.2×10^{-7}
30 MeV	3.2×10^{-4}	3.7×10^{-5}	1.3×10^{-6}	1.1×10^{-6}	2.5×10^{-7}
100 MeV	5.3×10^{-4}	4.7×10^{-5}	1.7×10^{-6}	1.5×10^{-6}	2.9×10^{-7}
300 MeV	4.1×10^{-4}	2.7×10^{-5}	9.9×10^{-7}	8.9×10^{-7}	1.5×10^{-7}
1 GeV	1.2×10^{-4}	6.9×10^{-6}	2.6×10^{-7}	2.4×10^{-7}	3.7×10^{-8}
30 GeV	1.7×10^{-5}	8.1×10^{-7}	3.3×10^{-8}	3.0×10^{-8}	4.9×10^{-9}
100 GeV	1.2×10^{-6}	5.4×10^{-8}	2.4×10^{-9}	2.1×10^{-9}	3.9×10^{-10}
300 GeV	6.4×10^{-8}	2.6×10^{-9}	1.3×10^{-10}	1.1×10^{-10}	2.3×10^{-11}
1000 GeV	2.9×10^{-9}	1.1×10^{-10}	6.2×10^{-12}	5.0×10^{-12}	1.2×10^{-12}

Table 5. Differential GCR fluxes for the most abundant elements for LIS for the theoretical maximum benchmarks

Differential GCR Flux (particles/(cm² sr s MeV/n)) for LIS, $\phi = 0$ MV					
Uncertainties are 10%-25%					
Energy/nucleon	Hydrogen	Helium	Carbon	Oxygen	Iron
10 MeV	2.6×10^{-1}	2.5×10^{-3}	8.8×10^{-5}	6.8×10^{-5}	2.3×10^{-5}
30 MeV	5.0×10^{-2}	7.7×10^{-4}	2.7×10^{-5}	2.2×10^{-5}	5.8×10^{-5}
100 MeV	9.4×10^{-3}	2.2×10^{-4}	7.9×10^{-6}	6.8×10^{-5}	1.4×10^{-6}
300 MeV	1.6×10^{-3}	5.4×10^{-5}	2.0×10^{-6}	1.8×10^{-6}	3.0×10^{-7}
1 GeV	2.2×10^{-4}	9.3×10^{-6}	3.5×10^{-7}	3.2×10^{-7}	4.9×10^{-8}
30 GeV	2.1×10^{-5}	9.2×10^{-7}	3.7×10^{-8}	3.4×10^{-8}	5.4×10^{-9}
100 GeV	1.3×10^{-6}	5.6×10^{-8}	2.5×10^{-9}	2.2×10^{-9}	4.0×10^{-10}
300 GeV	6.6×10^{-8}	2.6×10^{-9}	1.3×10^{-10}	1.1×10^{-10}	2.3×10^{-11}
1000 GeV	2.9×10^{-9}	1.1×10^{-10}	6.2×10^{-12}	5.1×10^{-12}	1.2×10^{-12}

Radiation Belts

For the radiation belt benchmarks, the main objective is to provide thresholds for the upper limit worst-case and 1-in-100-year fluxes at strategic locations. The locations are important because the radiation belts do not respond uniformly to strong driving, but individual populations and locations may respond differently to the same space weather event. Even at a single location, different portions of the energy spectra of worst-case fluxes are contributed by different events. Each is a spectrum of worst cases rather than a worst-case spectrum.

Estimates of the probability and severity of extreme flux events are obtained using extreme value theory (EVT). EVT analysis is aimed at characterizing the low-frequency tail of the probability distribution, which is not well represented by the “parent” probability distribution used to describe the full population of radiation belt flux observations. This parent distribution, which provides the probability that the flux will be less than or equal to a selected value, underestimates the value and/or frequency of the events in the low-frequency tail. Extreme value analysis constructs a separate probability distribution for the extreme tail. There are two main methods for EVT analysis: one involves block maxima, the other is based on exceedances over a high threshold. The “block maximum” method used by O’Brien et al. to calculate results in Table 6, divides the observations into non-overlapping time blocks of identical duration and takes the maximum flux value in each time block.¹⁶ The “exceedances over a high threshold” method, used by Meredith et al. for results in Table 6, takes all flux values in the distribution exceeding a specified threshold flux value.¹⁷ The resulting set of extreme flux values in each case is fit with a function to characterize the probability distribution in the low-frequency high-severity tail. Depending on the observations, the tail distribution can have an upper limit cut-off value, a power law fall off or an exponential fall off towards decreasing occurrence probabilities. Combining this with the parent probability distribution, an estimate of the radiation belt flux in a 1-in-100 year event, which has a 1% probability of occurring in any given year, is provided by the flux value at the 99th percentile. The flux value at the 100th percentile is an estimate of the worst-case flux or statistical maximum. O’Brien et al. find an upper limit flux cutoff in the low-frequency high-severity tail, which represents a true worst-case flux.

¹⁶ T. P. O’Brien et al., “Extreme Electron Fluxes in the Outer Zone,” *Space Weather* 5, no. 1 (January 2007), doi:10.1029/2006SW000240

¹⁷ N. P. Meredith et al., “Extreme Relativistic Electron Fluxes at Geosynchronous Orbit: Analysis of GOES $E > 2$ MeV Electrons,” *Space Weather* 13, no. 3 (March 2015): 170–184, doi:10.1002/2014SW001143

Table 6. Estimates of 1-in-100-year and statistical maximum electron radiation belt fluxes compared to the most extreme observed values

Location	Energy	Integral Electron Fluxes	
		1-in-100-Years (units = $\text{cm}^{-2} \text{s}^{-1} \text{sr}^{-1}$)	Most Extreme Observed (date) (units = $\text{cm}^{-2} \text{s}^{-1} \text{sr}^{-1}$)
GEO (GOES-West) ^a	>2 MeV	7.68×10^5	4.92×10^5 (7/29/2004 - 1 in 50 yrs)
GEO (GOES-East) ^a	>2 MeV	3.25×10^5	1.93×10^5 (7/29/2004 - 1 in 50 yrs)
		Worst Case (Statistical Maximum) (units = $\text{cm}^{-2} \text{s}^{-1} \text{sr}^{-1}$)	Most Extreme Observed (date) (units = $\text{cm}^{-2} \text{s}^{-1} \text{sr}^{-1}$)
HEO1 at L = 4.0 ^b	>8.5 MeV	$3.5 [1.7, 7.3] \times 10^2$	2.4×10^2 (8/30/1998)
	>4.0 MeV	$4.5 [1.7, 12] \times 10^4$	2.6×10^4 (8/5/2004)
	>1.5 MeV	$2.6 [2.2, 3.0] \times 10^5$	2.4×10^4 (8/30/1998)
HEO3 at L = 6.0 ^b	>630 keV	$1.0 [0.34, 3.3] \times 10^5$	6.0×10^4 (6/27/1998)
at L = 4.0	>630 keV	$4.5 [4.0, 5.1] \times 10^5$	4.3×10^5 (8/29/1998)
at L = 2.25	>630 keV	$2.1 [1.4, 3.1] \times 10^5$	1.9×10^5 (11/13/2004)
Location	Energy	Differential Electron Fluxes	
		1-in-100-Years (units = $\text{cm}^{-2} \text{s}^{-1} \text{sr}^{-1} \text{MeV}^{-1}$)	Most Extreme Observed (date) (units = $\text{cm}^{-2} \text{s}^{-1} \text{sr}^{-1} \text{keV}^{-1}$)
INTEGRAL /IREM at L [*] =6.0 ^c	2.05 MeV	1.58×10^5	1.4×10^5 (05/11/2016)
	1.82 MeV	1.76×10^5	-
	1.27 MeV	5.99×10^5	5.74×10^5 (05/11/2016)
	690 keV	4.68×10^6	4.60×10^6 (05/11/2016)
INTEGRAL/IREM at L [*] =4.5 ^c	2.05 MeV	5.79×10^5	5.65×10^5 (04/15/2006)
	1.82 MeV	7.29×10^5	-
	1.27 MeV	2.52×10^6	2.30×10^6 (04/15/2006)
	690 keV	1.46×10^7	1.42×10^7 (04/15/2006)
		Worst Case (Statistical Maximum) (units = $\text{cm}^{-2} \text{s}^{-1} \text{sr}^{-1} \text{MeV}^{-1}$)	Most Extreme Observed (date) (units = $\text{cm}^{-2} \text{s}^{-1} \text{sr}^{-1} \text{MeV}^{-1}$)
GEO (LANL) ^b	2.65 MeV	$5.9 [4.7, 7.3] \times 10^4$	5.1×10^4 (7/30/2004)
	625 keV	$4.1 [3.2, 5.2] \times 10^6$	3.4×10^6 (7/29/2004)
	270 keV	$2.0 [1.5, 2.6] \times 10^7$	1.6×10^7 (6/5/1994)

Location	Energy	Differential Electron Fluxes (<i>continued</i>)	
		Worst Case (Statistical Maximum) (units = $\text{cm}^{-2} \text{s}^{-1} \text{sr}^{-1} \text{MeV}^{-1}$)	Most Extreme Observed (date) (units = $\text{cm}^{-2} \text{s}^{-1} \text{sr}^{-1} \text{MeV}^{-1}$)
INTEGRAL/IREM at $L^* \approx 6.0^c$	1.82 MeV	1.98×10^5	-
	1.27 MeV	8.11×10^5	5.74×10^5 (05/11/2016)
	690 keV	4.82×10^6	4.60×10^6 (05/11/2016)
INTEGRAL/IREM at $L^* \approx 4.5^c$	2.05 MeV	6.08×10^5	5.65×10^5 (04/15/2006)
	1.82 MeV	8.10×10^5	-
	1.27 MeV	4.74×10^6	2.30×10^6 (04/15/2006)
	690 keV	1.51×10^7	1.42×10^7 (04/15/2006)

Notes: INTEGRAL/IREM is the Radiation Environment Monitor (IREM) on board the International Gamma Ray Astrophysical Laboratory (INTEGRAL) spacecraft, which is in an elliptical orbit with perigee of 9,000 km and apogee of 155,000 km. HEO1-HEO3 are three communication satellites in highly elliptical orbit with perigee of a few hundred kilometers and apogee of $\sim 7 R_E$.

^a Meredith et al., “Extreme Relativistic Electron Fluxes at Geosynchronous Orbit: Analysis of GOES $E > 2$ MeV Electrons.”

^b O’Brien et al., “Extreme Electron Fluxes in the Outer Zone.”

^c Meredith et al. (2017), “Extreme Relativistic Electron Fluxes in the Earth’s Outer Radiation Belt: Analysis of INTEGRAL IREM Data”, *Space Weather*, 15, 917-933, doi:10.1002/2017SW001651

1-in-100-Year and Worst-Case Electron Radiation Belt Fluxes

Studies of LANL geosynchronous or highly elliptical orbit (HEO) observations¹⁸ over one solar cycle or more suggest that the relativistic electron fluxes in GEO and HEO have upper limits—equivalent to 1-in-100-year fluxes—that do not vary with solar wind speed. Another study, using GOES-East and GOES-West fluxes over 19.5 years, does not find such an upper limit and speculates that confirming its existence would require a longer data set.¹⁹ All of these studies use extreme value analysis to get estimates of worst-case fluxes²⁰ or 1-in-10-year, -20-year, -50-year, -100-year, and -150-year fluxes.²¹

A more global estimate over energy and altitude of extreme integral flux values can be obtained using the statistical AE9 reference model. Figure 2 is a plot of the mean annual electron fluence from the statistical AE9 reference model. As indicated in the figure, the mean integral fluence at > 2 MeV in geostationary orbit is approximately 10^{12} cm^{-2} . Assuming the AE9 flux is constant and isotropic over 4π steradian over one year, the mean annual fluence would correspond to a flux of approximately $2.5 \times 10^3 (\text{cm}^2 \text{ s sr})^{-1}$. The estimated GOES West 1-in-100 year flux (approximately $7.68 \times 10^5 (\text{cm}^2 \text{ s sr})^{-1}$) is roughly 300 times larger than the AE9 flux. This can be used to develop a scaling factor for the AE9 model, which would then provide a crude estimate of the altitude distribution of 1-in-100 year fluxes with the

¹⁸ H. C. Koons, “Statistical Analysis of Extreme Values in Space Science,” *Journal of Geophysical Research* 106 (June 2001): A6, 10915–21, doi:10.1029/2000JA000234; O’Brien et al., “Extreme Electron Fluxes in the Outer Zone”; and G. D. Reeves et al., “On the Relationship Between Relativistic Electron Flux and Solar Wind Velocity: Paulikas and Blake revisited,” *Journal of Geophysical Research* 116 (February 2011): A2.

¹⁹ Meredith et al., “Extreme Relativistic Electron Fluxes at Geosynchronous Orbit.”

²⁰ Koons, “Statistical Analysis of Extreme Values in Space Science”; O’Brien et al. “Extreme Electron Fluxes in the Outer Zone.”

²¹ Meredith et al., “Extreme Relativistic Electron Fluxes at Geosynchronous Orbit.”

assumption that the energy spectra given by AE9 don't change with time or the level of magnetic activity. More sophisticated methodologies will be the subject of future updates to the benchmarks.

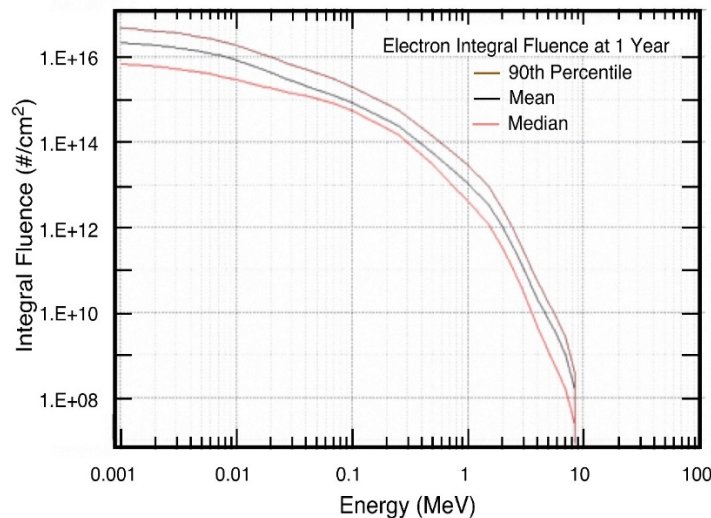


Figure 2. Integrated electron fluence versus energy in GEO from the AE9 model

Figure 2 shows the mean, median, and 90th percentile integral fluence from the AE9 model over the time interval of a year. The 1-in-100-year flux can be estimated from Figure 2 by dividing the mean integral fluence values by 4×10^8 to convert to units of $(\text{cm}^2/(\text{s sr}))^{-1}$, and then multiplying by 300 to scale the values to estimated 1-in-100-year flux levels indicated by GOES West observations.

Worst-Case <10s of KeV Substorm Electron Injections

One of the major causes of spacecraft anomalies is electrostatic discharge caused by electrical charges built up on satellite surfaces. Major sources of this surface charging are energetic electron injections produced by substorms. Substorm injections extend over a limited time interval (typically 1–2 hours) and cover regions that are localized in space. The electron flux at <100 keV energies within a substorm interval varies significantly on time scales of minutes. The relationship between the severity of the substorm activity and the energy spectra or flux of these energetic electron injections is not yet understood. Substorms occur during both magnetic storms and non-storm conditions. However, most of the largest auroral disturbances in the interval 1996–2012 as indicated by AL (< -3000 nT) or AU (> 1500 nT), listed in Nakamura et al.,²² occurred during major storm events and high-speed solar wind. Less severe but longer-lived intervals of substorm injections (and thus extended periodic enhancements of the magnetospheric electron environment) are associated with high-speed streams. An initial search of the scientific literature provided no estimates of extreme substorm flux values at relevant spatial and temporal scales.

1-in-100-Year Proton Radiation Belt Fluxes

The most significant energy ranges for proton radiation belts depends on the application of interest. For example, photovoltaics are lightly shielded with cover glasses, and proton degradation occurs

²² M. Nakamura et al., “Statistical analysis of extreme auroral electrojet indices,” *Earth, Planets and Space* 67 (2015): doi: 10.1186/s40623-015-0321-0

mainly from incident protons having energies less than 10 MeV. There is interest in higher energy protons. For example, electronics in the interior of spacecraft can degrade from cumulative exposure to protons, either from a total ionizing dose or displacement damage. High-energy protons can also cause single event effects in some of the more sensitive electronic devices.

A new empirical proton belt model (PolarP) characterizes trapped proton fluxes (protons/(cm²s MeV)) along medium Earth orbit (MEO) during nearly a full solar cycle from 2000 to 2010. The model is based on a statistical treatment of proton fluxes from the NASA Polar mission, operating over the period 1996–2007, which are further scaled along MEO using GPS ns41 observations. This scaling expands the energy range to include 50 keV–6 MeV and enables temporal features to be preserved. A more detailed description of the model is given by Chen et al.²³

The PolarP data set spans only ten years but can be used to derive a crude estimate of 1-in-100-year proton fluxes. Proton fluxes (with 24-second resolution) at all magnetic latitudes and L values between 2 and 4 were combined into a single probability distribution to improve the statistics in each energy bin of interest. The resulting probability distribution was scaled upward by a factor of ten to approximate the 100-year occurrence probabilities. The “low probability/high flux” tail of the distribution was fit with two functions, a truncated Gumbel function and a simple exponential function. The Gumbel probability distribution function is a particular case of the generalized extreme value distribution²⁴ function used to model extreme events. The ratio of the exponential/Gumbel fits provides a measure of the uncertainty. The 1-in-100 year fluxes based on the Gumbel fit are given in Table 7 with an estimate of the uncertainty.

Table 7. Estimates of 1-in-100-year proton radiation belt fluxes in the region L=2-4 including all magnetic latitudes.

Energy (MeV)	1-in-100-Year Proton Flux (protons/(cm ² s MeV)) based on Gumbel fitting function	Estimate of Uncertainty (ratio of exponential and Gumbel fit)
1	2.53 x 10 ¹⁰	~2
3	1.97 x 10 ¹⁰	~25
5	1.23 x 10 ⁸	~ 2
10	4.49 x 10 ¹⁰	~20

Source: Yue Chen, LANL

4. Caveats

Occurrence frequency analysis, which is currently the best technique for obtaining extreme value estimates for many of the ionizing radiation benchmarks, assumes that the physical processes that produced the available time series of a benchmark parameter are the same physical processes responsible for the occurrence of extreme events that fall in the distant tail of the probability distribution with low frequency but high intensity. It is possible that entirely different system-level behaviors (i.e., emergent processes or the chance interaction between two normally separated features within the system) may actually trigger extreme but rare events. In other words, an extreme event may

²³ Y. Chen et al., “Trapped Proton Environment in Medium-Earth Orbit (2000–2010),” Los Alamos National Laboratory (31 March 2016).

²⁴ The generalized extreme value distribution is a family of continuous probability distributions used in extreme value theory. For more information, see <https://gmao.gsfc.nasa.gov/research/subseasonal/atlas/GEV-RV-html/GEV-RV-description.html>

not just be a bigger version of a major event. This introduces uncertainty into an extrapolation based on fits to major but not extreme events.

As an example, the most extreme observed values of >2 MeV electron radiation belt fluxes in geosynchronous orbit (estimated to be a 1-in-50-year event) were observed on July 29–30, 2004. These extreme fluxes appeared not during an extreme magnetic storm event but after a sequence of three coronal mass ejections (CMEs) that were interspersed with high-speed solar wind hit Earth, producing progressively larger magnetic storms. The highest > 2 MeV electron fluxes at GEO occurred in the recovery phase of the third storm. The working hypothesis is that a rarefaction was produced between the leading edge of the high-speed solar wind and a faster moving CME ahead of it.²⁵ The rarefaction arrived as the outer belt was rebuilding, allowing the magnetospheric cavity to expand to an unusual size, providing an exceptionally large containment vessel for building the outer radiation belt.

In a second example, a preliminary simulation of a superstorm slightly larger than the Carrington event indicates that a major reconfiguration of the electron radiation belts is a possibility in a 1-in-100-year event.²⁶ When the boundary of the plasmasphere is pushed below 1.5 Earth radii (R_E) in the model and is no longer presenting a barrier through its role in enhanced losses, electrons in the outer belt are accelerated deeply inward to intensify the inner belt and deplete the outer belt. The region of the inner belt is home to the International Space Station and LEO satellites, which would be subjected to extreme levels of radiation for possibly years after the event in this scenario.

²⁵ Y. Miyoshi et al., “Flux enhancement of the outer radiation belt electrons after the arrival of stream interaction regions,” *Magnetospheric Physics*, 113 (2008): A3, doi:10.1029/2007JA012506

²⁶ Y. Shprits et al., “Profound change of the near-Earth radiation environment caused by solar superstorms,” *Space Weather*, 9 (2011): 8, doi:10.1029/2011SW000662

Benchmarks for Ionospheric Disturbances

1. Space Weather Action Plan 1.3.1

Action 1.3.1 of the Space Weather Action Plan states: “DOC and DOD, in coordination with NASA, DOI, NSF, and FCC, will: (1) assess the feasibility and utility of establishing functional benchmarks using the existing models and body of literature for this phenomenon; and (2) use the existing body of work to produce benchmarks.” It further states that “benchmarks and associated confidence levels will define at least the following:

- Ionospheric radio absorption and duration as a function of frequency;
- Total electron content (slant, vertical, and rate of change);
- Ionospheric refractive index; and
- Peak ionospheric densities and the height of the peak [of the layer].”

2. Ionospheric Disturbances

The ionosphere is highly variable and is driven externally by solar extreme ultraviolet (EUV) and X-ray irradiance, geomagnetic storms, and the neutral atmosphere. Figure 3 shows the approximate vertical profiles of the ionosphere electron density and the neutral atmosphere temperature for solar minimum and solar maximum daytime conditions. Ionospheric variability affects radio signal propagation by changing the reflection, refraction, absorption, and delay of the radio signal. The impact on radio signals depends on the vertical profile of the ionospheric electron density, and the angle of incidence of the radio wave on the ionosphere. The ionosphere can become turbulent due to small-scale irregularities that alter the amplitude and phase of transmitted signals. The term *ionospheric scintillation* is often used to describe this phenomenon.

Different layers in the ionosphere are labeled the D, E, and F regions as defined by the relative altitude above Earth’s surface. These layers transmit, absorb, reflect, and refract radio signals depending on the density of the layer and frequency of the radio wave. The signal delay of transionospheric signals is directly related to the total electron content (TEC), which is the number of electrons between the transmitter and receiver. For satellite navigation systems including Global Positioning Systems (GPS) and Global Navigation Satellite System (GNSS), a delay in arrival time results in positioning errors unless corrections are made. Strong horizontal gradients in the ionosphere can induce errors as the positioning information from each satellite varies with the TEC along the line of sight between the satellite and the receiver.

Three primary types of space weather phenomena affect the ionosphere and radio signal propagation. Solar flares enhance the low- and mid-latitude D region, essentially blocking high frequency (HF) communication on much of the dayside of Earth. Similarly, solar proton events enhance the D region at high latitudes, disrupting signal propagation and HF communication in polar regions. Geomagnetic storms modify the ionosphere in several ways, degrading satellite communication, navigation, and positioning capabilities, often on global scales. During an extreme storm, these effects on radio communication may extend to very high frequency (VHF) and ultra-high frequency (UHF). A very deep solar minimum with extremely low solar EUV irradiance could also affect HF communication and radar systems, but these conditions will be discussed in future updates to the benchmarks document. A brief discussion of these extreme space weather conditions and their potential effects on the ionosphere follow.

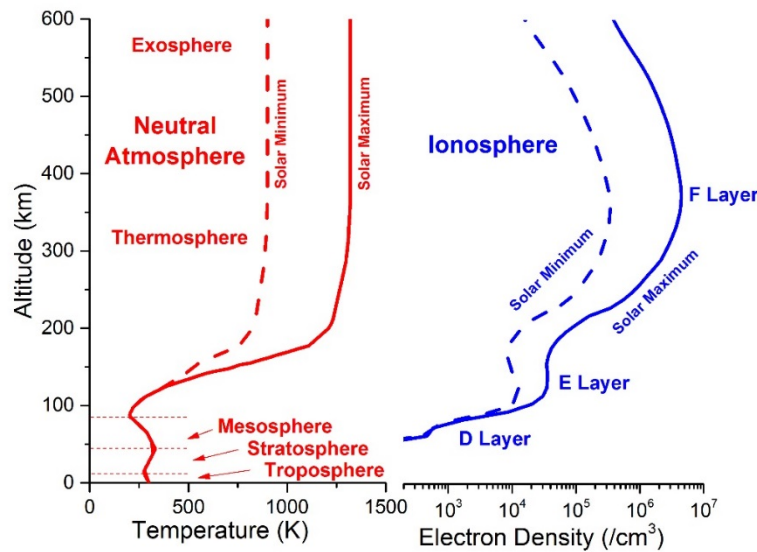


Figure 3. Height profiles of the neutral atmosphere temperature and the ionosphere electron density for daytime solar minimum and solar maximum conditions (layers of the neutral atmosphere and ionosphere are labeled for reference)

Solar Flares

Solar X-ray photons penetrate to the lower part of the ionosphere, or D region of the ionosphere (60–90 kilometers) creating a narrow enhanced layer that absorbs HF radio waves (3–30 megahertz [MHz]), affecting maritime sea-to-shore services, over-the-horizon radar systems, Global Maritime Distress and Safety System communications, and several other military and government communication systems. The stronger the solar flare, the more enhanced the D region, the larger the affected area, and the higher the affected radio frequency. For an extreme flare (e.g., a flare classified as X30 or greater, in a classification system where X is the highest class), the D region would completely absorb HF radio signals up to about 40 MHz or higher on much of the dayside of Earth. Solar X-ray flares typically last for tens of minutes, but the EUV portion of the flare can last 1–3 hours. The effects on HF communication last as long as the solar X-ray flux levels remain high.

Flare effects on the D region are well understood, and the empirical models used to specify these effects work well for moderate and large flares. The relationship between flare magnitude and HF radio frequency is empirical, and extreme X-ray flares (> X30) have never been accurately observed or recorded.²⁷ Thus, a number of uncertainties exist in determining not only the magnitude of the largest possible flare, but also the response of the D region and the subsequent impact on HF propagation. Flares can modify other regions of the ionosphere, but these effects are relatively small compared to other variations caused by geomagnetic storms and solar cycle variations. Flares are sometimes associated with radio emissions at frequencies near the GPS frequencies and could potentially affect communication and navigation systems (as discussed in Action 1.4 of the Space Weather Action Plan).

²⁷ For example, see N. R. Thomson, C. J. Rodger, and R. L. Dowden, “Ionosphere Gives Size of Greatest Solar Flare.” *Geophysical Research Letters* 31 (2004): L06803.

Solar Energetic Protons

Energetic protons, accelerated near the Sun and in the solar wind by solar eruptive events such as coronal mass ejections (CMEs) and flares, are guided by the geomagnetic field and penetrate to the lower D region of the high-latitude ionosphere, creating a narrow enhanced layer that, like the enhancement caused by solar flares, absorbs radio waves. During large geomagnetic storms, the affected regions extend towards the equator. In an extreme storm, the proton effects on communication may reach ± 25 degrees geomagnetic latitude from the magnetic pole. The effects of protons on the ionosphere and on communication are well understood and can be predicted, assuming the energy distribution of the precipitating protons is known. Proton events can last for several days, and the loss of HF communication from these events may last just as long. An extreme solar proton event may disrupt HF communications at high latitudes for a week or more. Protons do not change the other parts of the ionosphere where the bulk of the electrons reside; therefore, the impact of solar proton events on the ionosphere is limited.

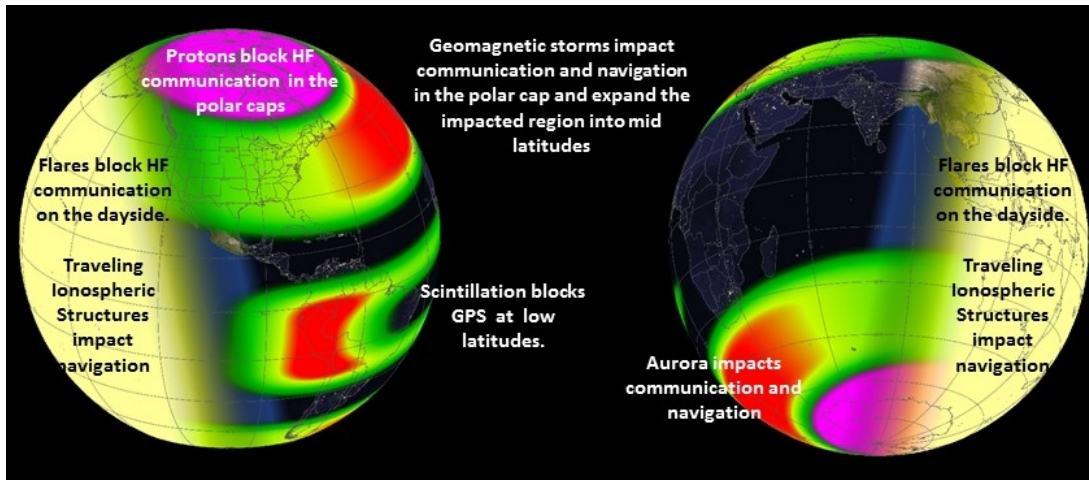
Geomagnetic Storms

Extreme geomagnetic storms, which are usually caused by CMEs, have complex and different effects on the ionosphere at high, mid-, and low latitudes. The auroral effects associated with geomagnetic storms increase ionospheric density and heat and expand the thermosphere. The auroral zone moves toward the equator, and the equatorial ionospheric scintillation region can expand toward the poles, bringing the ionospheric structures, which are prevalent in the equatorial and polar regions, to mid-latitudes. Auroral particles and current systems deposit energy into the ionosphere-thermosphere system, which, in turn, creates structures such as waves, gradients, and traveling ionospheric disturbances that enhance the variability of the mid-latitude ionosphere and disrupt HF through VHF signal propagation. The effect on GPS navigation of the resulting sharp electron density gradients can be quite severe and can last for hours or even days.²⁸ At low latitudes, ionospheric irregularities and plasma bubbles interfere with satellite communication, navigation, positioning, and radar systems that depend on trans-ionospheric radio links. These structures can be enhanced during geomagnetic storms (e.g., if the storm creates higher than normal plasma vertical uplift).

One additional consideration is the possibility of several simultaneous events, due to repeated eruptions from the same active region on the Sun, which is common. During major geomagnetic storms, solar flares, protons, X-rays, and radio bursts are likely to occur simultaneously over the course of several days. The severity and extent of their effects will depend on solar activity, the season, and the state of the system at the onset of the storm. Some of the effects on the ionosphere may be additive, but non-linear effects are common and are not fully understood. The ionosphere is tightly coupled to the thermosphere and magnetosphere, which also respond to solar activity and further influence the response of the ionosphere.

Figure 4 shows an estimate of the global extent of the various ionospheric disturbances during extreme space weather conditions.

²⁸ A. J. Mannucci et al.. "Dayside Global Ionospheric Response to the Major Interplanetary Events of October 29–30, 2003 Halloween Storms." *Geophysical Research Letters* 32, no. 4 (May 2005): L12S02; Rodriguez Bilbao et al. "Precise point positioning degradation in the presence of a SITEC." *2015 1st URSI Atlantic Radio Science Conference (URSI AT-RASC) (2015): 1-1*. doi: 10.1109/URSI-AT-RASC.2015.7303132



Source: From a private communication with Air Force Research Laboratory staff member.

Figure 4. Estimate of the global extent of various ionospheric disturbances during extreme space weather conditions

Table 8 provides descriptions of some of the phenomena described here and their effects on the ionosphere.

Table 8. Effect of extreme events on the ionosphere

Phenomenon	Event	Location	Environmental Effect
Flare	D Region Enhancement	Sunlit side of Earth	Absorbs RF signals from HF to VHF in the lower ionosphere
Energetic Protons	D Region Enhancement	High and mid-latitudes	Absorbs RF signals from HF to VHF in the lower ionosphere
Geomagnetic Storms	Polar Cap and Aurora	High and mid-latitudes	Patches, plasma structures, and ionospheric gradients refract radio waves.
	Traveling Ionospheric Disturbances and Storm-Enhanced Densities	Mid-latitude region on the dayside of Earth	Creates large TEC enhancements (up to 200 TEC units) and strong gradients in TEC
	Equatorial Scintillation	Latitudes ± 20 degrees of geomagnetic equator	Large-scale plasma depletions and associated small-scale ionospheric structures observed just after sunset and generally up to midnight. Scintillation of transmitted radio signals.

3. Methodology for Establishing Benchmarks for Ionospheric Disturbances

A number of parameters are used to describe the ionospheric properties that typically affect communication, navigation, and positioning. In addition to the TEC, these parameters include the highest affected frequency (HAF), the maximum usable frequency (MUF), the height in kilometers of the F₂ layer (hmF₂), the peak density of the F₂ layer (NmF₂), as well as the phase and amplitude scintillation

indices Sigma-Phi and S4.²⁹ Global maps of each of these parameters would fully describe the extreme event impacts on communication, navigation, and positioning systems.

The ionospheric response to flares and proton events is reasonably well understood and predictable. It is possible to quantify the impacts of severe solar flares and extreme solar energetic proton events on HF communication. Empirical models driven by solar X-ray data and energetic proton data (from GOES), geomagnetic activity (from U.S. Geological Survey and Defense Meteorological Satellite Program magnetometers), and solar wind, interplanetary magnetic field (IMF) data (from ACE and the Deep Space Climate Observatory [DSCOVR]) provide reasonable estimates of the ionospheric response and the effects resulting from extreme events. The ability of current empirical models to predict extreme conditions is uncertain because they reflect only what has been observed previously; however, reasonable estimates may be readily achievable.

The ionospheric response to extreme geomagnetic storms is much more complex. Because it is not yet fully understood how extreme solar wind conditions propagate through the magnetosphere, it is difficult to characterize the resulting modifications to the ionosphere. Conditions associated with high-latitude and equatorial scintillation are not well captured in most models. Ionospheric features, such as traveling ionospheric disturbances and irregularities and storm enhancements in plasma density, may have severe effects on technologies that are difficult to predict. The ionospheric effects on systems could be specified by a detailed analysis of storm conditions that have been observed and additional research and development to couple physics-based ionospheric models with magnetosphere and thermosphere models.

Extreme events are difficult to define given only a few decades of data. An extremely large storm occurred in 1859 (the Carrington event), but there were few measurements of the space environment at that time. There are extensive observations of more recent storms, such as those in March 1989, July 2000, June 2001, and October-November 2003, all of which were significant, but these events do not necessarily represent a 1-in-100-year storm. Estimates of the magnitude of space weather parameters during the Carrington event are shown in Table 9, along with the largest observed events from more recent records. This table references the Disturbance Storm Time (Dst)³⁰ index as a measure of the geomagnetic activity.

Table 9. Magnitude of the largest space weather storms

Phenomenon	Carrington Event (Estimates)	Largest Observed
Flare	X35 to X45	X28-X45 (estimated) ^a
Proton Event	2.7 to 11.0 × 10 ⁹ protons cm ⁻² @30 MeV	10 × 10 ¹⁰ protons cm ⁻² @30 MeV ^b
Geomagnetic Storm	Dst -900 to -1760 nT	Dst -589 nT ^c

^a November 2003; GOES XRS saturated so flare magnitude is an estimate (e.g., Thomson, Roger, and Dowden, "Ionosphere Gives Size of Greatest Solar Flare").

^b Proton flux observed at 30 MeV for the August 1972 event

^c March 1989.

²⁹ S. Basu et al., "250 MHz/GHz Scintillation Parameters in the Equatorial, Polar and Auroral Environments," *IEEE Transactions on Selected Areas in Communications*, SAC-5 (1987): 102-115.

³⁰ M. Sugiura, "Hourly Values of Equatorial Dst for the IGY." In *Annals of the International Geophysical Year*, Part 1: 9-45 (Pergamon Press, 1964).

Although much is known about the local characteristics of the ionosphere that change in response to geomagnetic storm conditions, it is still difficult to quantify the global response to an extreme storm. Earth's ionosphere is a dynamic system that is strongly coupled to both the magnetosphere and the neutral atmosphere. Estimating the ionospheric response to extreme geomagnetic storms is informed by an understanding of the entire magnetosphere-ionosphere-thermosphere (MIT) system. The current uncertainties on estimating this benchmark are very large. The larger scale responses could be twice what has been observed to date, whereas features such as gradients could be 10 times larger if they are localized and cover a smaller region. It is also possible that the response to an extreme event is actually no greater than what has been observed during some of the largest storms (e.g., the large geomagnetic storms of October 2003, referred to as the Halloween storm,³¹ or of July 2000, referred to as the Bastille Day storm³²).

It will be important to take advantage of available data from observations from previous large storms, ground-based GPS and magnetometers, GOES and DSCOVR missions, and the multi-national COSMIC constellation of satellites. Solar, solar wind, and magnetosphere observations will play key roles in the data analysis as well. Analysis of these observations will provide a sound basis for estimates of the extreme conditions on the Sun and in the solar wind, including solar EUV and X-ray irradiance as well as solar wind speed, density, and the IMF. Other variables include the state of the thermosphere/ionosphere at the beginning of the storm, the Universal Time Coordinated start of the storm, and to some extent, the wave field (tides, planetary waves, and gravity waves) propagating from the lower atmosphere. Once the ranges of all the input drivers are determined, these drivers can be fed into models of the MIT system. It may then be possible to model the range of responses in the ionosphere to extreme events, but new phenomena, such as non-linear effects, may not be captured adequately by current models.

The equatorial ionosphere responds to changes in geomagnetic activity, but it is not as tightly coupled to geomagnetic storm drivers as high- and mid-latitude regions. At low latitudes, the effects are typically due to penetration electric fields, whereas responses at high latitudes are more complex. Under extreme conditions, the extent of equatorial ionospheric scintillation could expand both in local time and in latitude. The number and intensity of the plasma bubbles could also increase, thus expanding and amplifying the phenomena and their effects on navigation and communication systems.

4. Benchmarks

Because of the complexities in modeling ionospheric disturbances, no quantitative benchmarks were set for this section. Although much is known about the local characteristics of the ionosphere that change in response to geomagnetic storm conditions, it is still difficult to quantify the global response to an extreme storm. Earth's ionosphere is a dynamic system, and is strongly coupled to both the magnetosphere and the neutral atmosphere. A better understanding of the entire MIT system and its response to extreme geomagnetic storms would help inform this benchmark. Providing benchmark estimates of various extremes in the ionospheric parameters with uncertainties approaching 100% could potentially be misleading and may lead to severe under or over estimation of disturbances to the

³¹ S. Basu et al., "Response of the Equatorial Ionosphere to Prompt Penetration Electric Fields during Intense Magnetic Storms," *Journal of Geophysical Research* 112 (2007): A08308. doi:1029/2006JA012192

³² S. Basu et al., "Response of the Equatorial Ionosphere in the South Atlantic Region to the Magnetic Storm of July 15, 2000," *Geophysical Research Letters* 28, no. 3 (2001): 577.

ionosphere. Phase 2 of the benchmarks effort (NSWAP 1.3.3) will seek to refine the benchmark values and uncertainties.

In the absence of benchmarks, measured values from the intense 2003 Halloween event for ionospheric disturbances are reported here. Mannucci reports a vertical TEC of 250 TECu (where 1 TECu = 1×10^{16} electrons m^{-2}) with an associated error of approximately 3 TECu, and Datta-Barua reports a TEC spatial range gradient of 40 cm/km and a TEC temporal range gradient of 15 cm/s.^{33,34,35} These conditions could last up to several days.³⁶

³³ A.J. Mannucci, "Global Ionospheric Storms," white paper submitted to the Space Studies Board of the U.S. National Research Council for its 2010 "decadal survey" in solar and space physics (heliophysics), 2010.

³⁴ P. Stephens et al., "New leveling and bias estimation algorithms for processing COSMIC/FORMOSAT-3 data for slant total electron content measurements," *Radio Science* 46 (2011): RS0D10. doi: 10.1029/2010RS004588

³⁵ S. Datta-Barua, "Ionospheric Threats to Space-Based Augmentation System Development," presented at the Proceedings of the 17th International Technical Meeting of the Satellite Division of The Institute of Navigation (ION GNSS 2004), Long Beach, California, 2004.

³⁶ M. Hapgood et al., *Summary of Space Weather Worst-Case Environments*, RAL technical report, Revised edition, RAL-TR-2016-006, May 2016.

Benchmarks for Solar Radio Bursts

1. Space Weather Action Plan 1.4.1

Action 1.4.1 of the National Space Weather Action Plan states: “DOC, DOD, and NASA, in coordination with DOI and FCC, will: (1) assess the feasibility and utility of establishing functional benchmarks [for solar radio bursts] using the existing models and body of literature for this phenomenon; and (2) use the existing body of work to produce benchmarks [for solar radio bursts].”

2. Solar Radio Bursts

Solar radio bursts are emitted from the Sun during solar flares; on average, solar flares occur every 3.5 days at solar maximum and every 18.5 days at solar minimum. Solar radio bursts are significant because use of the radio spectrum has become as ubiquitous as the use of electricity. The Nation relies on the radio spectrum in so many ways that it is impossible to enumerate them all or to completely understand how disruptive disturbance to the radio spectrum could be. Note the radio bursts considered here include those from flare-associated phenomena, including coronal mass ejections, thus covering all the bright emissions likely to impact users of the radio spectrum.

In a review of Federal radio uses, the DOC National Telecommunications and Information Administration (NTIA) looked at frequency ranges from low frequency (30 kilohertz [kHz]) to extra high frequency (300 gigahertz [GHz]).³⁷ The list of uses is extremely broad and includes such diverse areas as air traffic control, radio navigation, ship safety and security, space, law enforcement, environmental monitoring, and national defense.

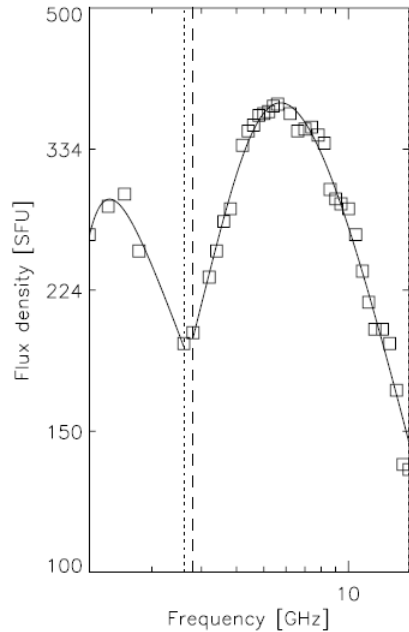
3. Methodology for Establishing Benchmarks for Solar Radio Bursts

The most extensive data set on solar radio bursts is the U.S. Air Force’s Radio Solar Telescope Network (RSTN), with data from 1960 up to the present. The RSTN network is a global network of stations, thus ensuring continuous observations of the Sun. The RSTN data have observations over all of the frequency bands of interest, making it the ideal data set for setting benchmarks. The next best data source is the Nobeyama Radio Observatory, which observed for 45 years only in the higher frequency bands (>1000 MHz) from a single site, thereby missing any bursts occurring after sunset. These data can be used as a consistency check against any analysis performed with the RSTN data.

The main users of the radio spectrum that can be affected by solar events can be sorted into the standard frequency bands of VHF, UHF, and microwaves. In addition, due to their common usage, GPS frequencies and the $F_{10.7}$ index (2800 MHz) are specifically highlighted.

Figure 5 shows the spectrum for a typical radio burst. Note the two peaks in the spectrum with a minimum around 2–3 GHz. Figure 5 does not provide an instantaneous view of a radio burst; the radio burst spectrum varies significantly both within a burst and from burst to burst.

³⁷ Department of Commerce (DOC), *Federal Radar Spectrum Requirements*, National Telecommunications and Information Administration (NTIA), NTIA Special Publication 00-40, May 2000.



Source: G. M. Nita, D. E. Gary, and L. J. Lanzerotti, "Statistics of Solar Microwave Radio Burst Spectra with Implications for Operations of Microwave Radio Systems." *Space Weather* 2 (2004): S11005, Figure 1.

Figure 5. Typical radio spectrum burst

For the 1-in-100-year benchmarks, the results presented in Nita et al. were used.³⁸ Defined frequency bands that align with standard usage for the benchmarks were chosen, whereas Nita et al. and the RSTN data are at discrete frequencies within each band. The benchmarks can be assumed to be valid over the full range of frequencies covered by a band. In cases where multiple discrete frequencies fall within a single band, the largest computed intensity was used as the benchmark.

Three different emission mechanisms are important in assessing the theoretical maximum intensity expected from solar radio bursts. Theoretical maximum intensities for microwave frequency bands (4,000–20,000 MHz) are the most straightforward to compute, because these are dominated by synchrotron emission, which are incoherent emissions produced by electrons accelerated in solar flares. The radio flux from a burst source can be expressed as the product of the effective brightness temperature of the source and its area, scaled by the square of the frequency. These factors can be estimated and used to derive a frequency-dependent theoretical maximum.

At lower frequencies, the situation is more complicated because the two emission mechanisms active there are coherent, and placing upper limits on their effective brightness temperatures is difficult. Between 600 MHz and 3 GHz, covering the range of UHF, GPS, and F_{10.7}, electron cyclotron maser emissions can operate with very high brightness temperatures (e.g., 10¹⁴ K), albeit with upper limits likely to be similar to the source size. At frequencies below 600 MHz (the band), the plasma emission mechanism from the conversion of Langmuir waves dominates, again with the potential for very high brightness temperatures, but also with the potential for much larger source sizes.

³⁸ G. M. Nita et al. "The Peak Flux Distribution of Solar Radio Bursts." *Astrophysical Journal* 570 (May 2002): 423–438.

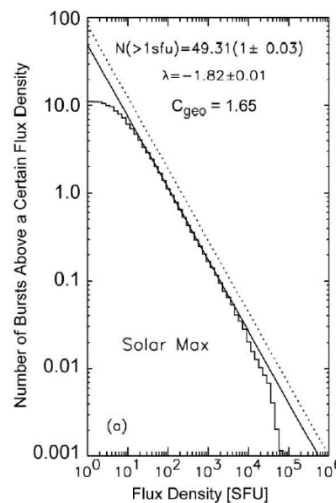
4. Benchmarks

Table 10 shows 1-in-100-year benchmarks for solar radio bursts. These Phase 1 benchmarks are obvious overestimates. This is because both the Nita et al. paper and the 2012 paper with Nobeyama data³⁹ show that the frequency of radio bursts falls off much more rapidly than a simple linear extrapolation implies. Inspection of the plots in Figure 5 (above) and Figure 6 (below) indicate the phase 1 benchmarks overestimate the 1-in-100-year flux by at least an order of magnitude. The 1-in-100-year benchmarks were derived by extrapolating the power-law fits in Nita et al. (the solid and dashed (corrected) lines) to an event rate of 1 event every 36,525 days, or 2.7379×10^{-5} events per day.

Table 10. Benchmarks for solar radio bursts

Frequency Band Name	Frequency Band (MHz)	1-in-100-Year Benchmark (sfu) ^a	Error Bars (sfu) ^a	Theoretical Maximum
Very High Frequency (VHF)	30–300	2.8×10^9	$[-2.5 \times 10^9, +0]$	Phase 2
Ultra High Frequency (UHF)	300–3,000	1.2×10^7	$[-1 \times 10^7, +0]$	Phase 2
Global Positioning System (GPS)	1,176–1,602	1.2×10^7	$[-1 \times 10^7, +0]$	Phase 2
F _{10.7}	2,800	1.3×10^7	$[-1 \times 10^7, +0]$	Phase 2
Microwave	4,000–20,000	3.7×10^7	$[-2.5 \times 10^9, +0]$	Phase 2

^a Solar flux is measured in watts (W) per square meter (m²) per hertz (Hz), with 1 solar flux unit (sfu) equal to 10^{-22} W m⁻² Hz¹.



Source: G. M. Nita et al., “The Peak Flux Distribution of Solar Radio Bursts.” *Astrophysical Journal* 570 (May 2002): 423–438, Figure 10(a).

Figure 6. Cumulative number of bursts per day at frequencies above 2 GHz during solar maximum years

³⁹ Q. Song, G. Huang, and B. Tan, “Frequency Dependence of the Power-Law Index of Solar Radio Bursts.” *Astrophysical Journal* 750 (May 2012): 160–163.

No theoretical maximum benchmarks were computed because no published work addresses the question of the theoretical maximum intensity expected from solar radio bursts.

To assess the theoretical maximum intensity expected from solar radio bursts, it is important to note that there are three different emission mechanisms that play a role and are typically dominant in different frequency bands. The radio flux from a burst source can generally be expressed as the product of the effective brightness temperature of the source and its area, scaled by the square of the frequency. The key to identifying the theoretical maximum in each frequency band is the ability to determine the maximum feasible brightness temperature and area.

Theoretical maximum intensities for the microwave frequency bands (4-20 GHz) are the most straight-forward to compute, but at lower frequencies the situation is more complicated because the two emission mechanisms active there are coherent, and it is difficult to place upper limits on their effective brightness temperatures. An estimate of the maximum brightness temperature of plasma emission may be possible upon further investigation of the literature.

With the current state of knowledge, we therefore believe that we can provide plausible theoretical maxima at high and low frequencies, with somewhat less certainty in the UHF-GPS-F10.7 frequency bands.

Benchmarks for Upper Atmosphere Expansion

1. Space Weather Action Plan 1.5.1

Action 1.5.1 of the National Space Weather Action Plan states: “DOC, DOD, NSF, and NASA, in coordination with DOI and FCC, will: (1) assess the feasibility and utility of establishing functional benchmarks [for upper atmosphere expansion] using the existing models and body of literature for this phenomenon; and (2) use the existing body of work to produce benchmarks [for upper atmosphere expansion].”

2. Upper Atmosphere Expansion

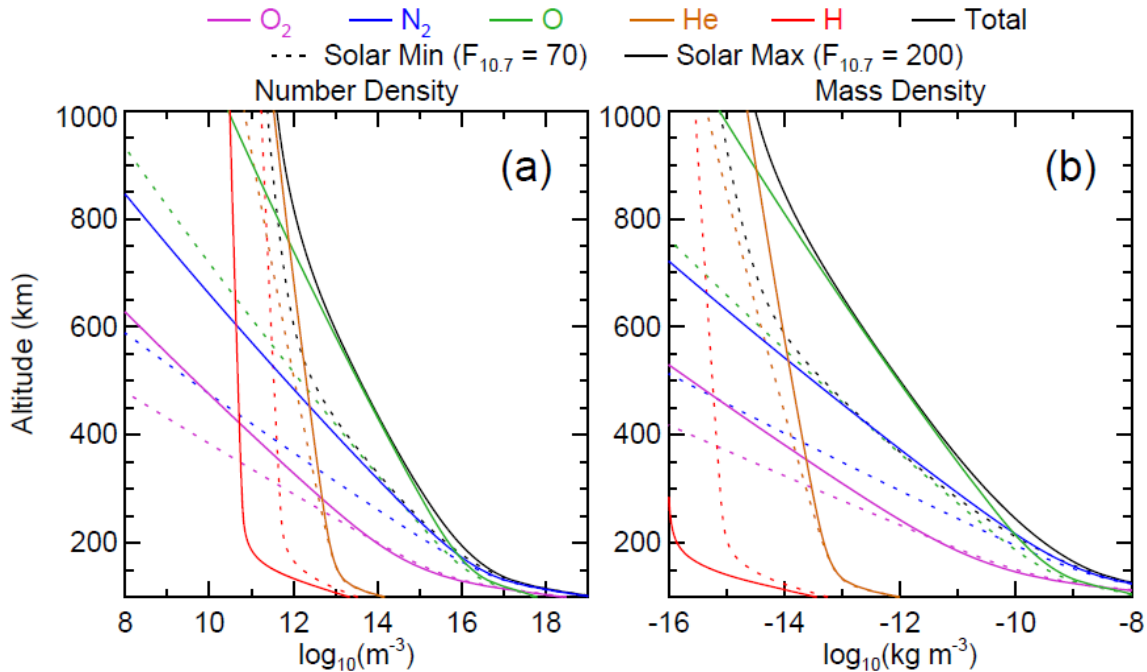
Upper atmosphere expansion refers to changes in the thermosphere that can affect satellite drag at low Earth-orbit (LEO).⁴⁰ The primary effect arises from an increase in temperature, which causes an increase in neutral density at a fixed altitude in Earth’s upper atmosphere; temperature is therefore considered synonymous with density for the purposes of the benchmark. Figure 3 (in the section on benchmarks for ionospheric disturbances) illustrates the vertical profile of the atmospheric temperature with the layers of the atmosphere labeled. Upper atmospheric heating can be driven by solar or geomagnetic activity. The neutral density response also depends on neutral composition. Composition varies as a function of altitude and solar cycle. At 400 kilometers, the thermosphere at mean levels of solar activity is dominated by atomic oxygen (O). At 250 kilometers molecular nitrogen (N₂) contributes a significant fraction, and at 850 kilometers helium (He) begins to dominate.

Figure 7 shows the vertical profile of the number densities (a) and mass density (b) of the atmospheric species from 100 to 1000 kilometers altitude for low solar activity (dashed lines) and high solar activity (solid lines). The relative composition of species at a fixed altitude is also dependent on the level of solar activity, as the atmosphere expands and contracts. To reflect this altitude dependence, the Benchmarks consider the environmental conditions and response to energy injection at three height levels: 250 kilometers, 400 kilometers, and 850 kilometers. While assets at 850 kilometers are not typically considered vulnerable to significant satellite drag force magnitudes, the variability in these forces may still constitute the largest contribution to overall orbital errors and drag effects above 700 kilometers altitude during storms have been reported. Moreover, during extreme events the neutral density experienced at 850 kilometers during storms would be comparable to the drag at 600 kilometers altitude during quiet times. In addition, during extreme storms at higher altitudes, ions can become a significant component of the atmosphere causing drag in addition to the neutrals.

At these altitudes, 250 kilometers, 400 kilometers, and 850 kilometers, neutral species (e.g., N₂, O, He) tend to dominate. However, at 850 kilometers altitude the ionized atmosphere can contribute a significant fraction (a few percent) of the total density and impacts drag just as a neutral constituent would. In addition, the ions can be transported to higher altitudes not just by thermal expansion, but also through transport by electric fields. During an extreme geomagnetic storm, vertical plasma drift at low and mid latitudes are expected to exceed 200 m/s, which if present for an hour or two, could raise the relative density concentration of the ionized atmosphere at 850 kilometers to greater than 10%. To date, there has been no direct evidence that the vertical motion of the ions driven by prompt penetration electric fields has an appreciable effect on vertical transport of neutral density. Quantifying

⁴⁰ J. T. Emmert, “Thermospheric Mass Density: A Review,” *Advances in Space Research* 56 (2015): 773–824; NRC, *Orbital Debris: A Technical Assessment* (Washington, D.C.: National Academies Press, 1995); NRC, *Continuing Kepler’s Quest: Assessing Air Force Space Command’s Astrodynamics Standards* (Washington, D.C.: National Academies Press, 2012).

the impact of the ionized atmosphere on the drag of satellites and orbital prediction of debris will be considered in Phase 2.



Source: T.J. Fuller-Rowell et al. "How the Thermosphere and Ionosphere Might React to an Extreme Space Weather Event," *Extreme Events in Geospace*. Edited by N. Buzulukova. Elsevier Inc., Cambridge, MA, 2017.

Figure 7. The vertical profile of the number densities (a) and mass density (b) of the different atmospheric species from 100 to 1000 kilometers altitude for low solar activity (dashed lines) and high solar activity (solid lines)

In-track winds change apparent density along an orbit, and cross-track winds influence orbit trajectory. The benchmark therefore considers neutral density, and winds, as the primary parameters impacting satellite drag during extreme events. The additional impact of possible ion density enhancements on total density at higher altitude will be considered in Phase 2.

Neutral density and winds at LEO altitudes pose two distinct risks to operational spacecraft:

1. The direct effect of enhanced drag on the spacecraft, changing its orbit, increasing the uncertainty of its position, and reducing its orbital lifetime.
2. The indirect effect of atmospheric expansion and winds on the ability to monitor the trajectories of debris, including objects with high area-to-mass ratios, for collision avoidance.

The issue of the predicting the orbits of debris is of particular concern for collision avoidance. Debris objects tend to be much smaller than operational satellites, some have a larger area-to-mass ratio, have eccentric orbits that are affected by thermosphere horizontal and vertical structure, and consequently are more diversely affected by atmospheric drag. Collision avoidance has become of increasing concern due to the recent proliferation of space debris in LEO. One cause of the rapid inflation in the number of objects was the collision of one of the satellites in the Iridium constellation with a spent Russian satellite COSMOS 2251. Incidents like this create a large cloud of debris.

The issue of space debris, which has been brought to a new level of awareness, highlights the need for accurate orbit predictions and tracking of space objects. The Space Surveillance Network (SNN) currently tracks more than 20,000 objects greater than 10 cm. These objects consist of everything from active satellites, defunct satellites, and spent rocket stages, to smaller debris arising from erosion, explosion, and collision fragments. Since the orbits of these objects often overlap the trajectories of newer operational spacecraft, collision of the debris with active satellites is of serious concern.

The number of objects in may reach a critical density where the creation of new debris occurs faster than various natural forces can remove them from orbit. Beyond this point, a runaway chain reaction can occur that quickly reduces all objects in orbit to debris in a phenomenon known as the Kessler Syndrome.⁴¹ The biggest uncertainty in orbit prediction in low Earth orbit is estimating the likely drag on the satellite due to neutral density in the upper atmosphere. The long-term trend of reduced density in the upper atmosphere due to carbon dioxide (CO₂) cooling⁴² will tend to increase the lifetime of debris and exacerbate the issue of collision avoidance.

The upper atmosphere expansion benchmark quantifies the response to three main sources driving upper atmospheric density or winds. These are:

1. Ultraviolet radiation from the Sun, which is produced continuously and changes day-to-day;
2. Ultraviolet radiation from the Sun, which is produced by a solar flare transient event; and
3. Coronal mass ejections from the Sun, which are transient events driving geomagnetic storms.

3. Methodology for Establishing Benchmarks for Upper Atmosphere Expansion

The methodology for establishing the benchmarks is described for the three main causes of upper atmosphere expansion:

1. The impact from extreme solar ultraviolet (EUV; wavelength < ~100 nm) radiation and far ultraviolet (FUV; wavelengths > 100 nm) radiation on the upper atmosphere on timescales greater than one day;
2. EUV enhancement of the upper atmosphere during impulsive events, such as solar flares; and
3. CMEs that drive geomagnetic storms that lead to the expansion of the upper atmosphere.

⁴¹ D. J. Kessler and B. G. Cour-Palais, "Collision Frequency of Artificial Satellites: The Creation of a Debris Belt," *Journal of Geophysical Research* 83 (1978): A6, 2637–2646, doi:10.1029/JA083iA06p02637

⁴² J. Emmert, J. Picone, S. Lean, and S. Knowles, "Global Change in the Thermosphere: Compelling Evidence of a Secular Decrease in Density," *Journal of Geophysical Research* 109 (2004); R. Akmaev and V. Fomichev, "Cooling of the Mesosphere and Lower Thermosphere Due to Doubling of CO₂," *Annales Geophysicae* 16 (1998): 1501–1512.

Effects of Solar Extreme Ultraviolet (EUV) and Far Ultraviolet Radiation (FUV) on Upper Atmosphere Expansion on Timescales Greater than One Day

This benchmark uses the NRLMSISE-00 empirical neutral density model.⁴³ Alternative empirical models such as JB2008⁴⁴ or DTM-2013⁴⁵ could equally be used. The accuracy of the available empirical models is similar, all having been constructed with similar observed neutral density or tracking data. During quiet times, their accuracy is ~20% increasing to ~50% during geomagnetic storms. Their uncertainty is expected to increase further when extrapolating for extreme events, to ~100%, since clearly no observational data is available during these times. Empirical neutral density models of the effects of solar EUV and FUV on upper atmosphere expansion are driven by proxies, such as the average of the daily solar 10.7-centimeter solar radio flux ($F_{10.7}$) and its 81-day mean. The $F_{10.7}$ radio emission originates high in the chromosphere and low in the corona of the solar atmosphere; it correlates well with the number of sunspots as well as ultraviolet (UV) fluxes.⁴⁶ Since thermospheric neutral winds do not increase substantially in response to increases in solar ultraviolet radiation, the benchmark for this category is restricted to neutral density.

The benchmarks are defined relative to the NRLMSISE-00 empirical neutral density reference model in order to extrapolate the response to a 1-in-100-year and theoretical maximum event. Benchmark values are determined assuming the enhanced ultraviolet flux has persisted for at least 1 to 5 days, guided by the fact that the neutral density response to EUV has an e-folding time (interval for an exponentially growing quantity to increase by expansion factor e) of about 1 day, and the response to the longer FUV wavelengths that penetrate more deeply into the upper atmosphere is 3 to 5 days.

Over the past 68 years, the daily $F_{10.7}$ at 1 AU exceeded 300 solar flux units (sfu)⁴⁷ on only 80 days (0.3 percent occurrence rate). The peak value of the daily $F_{10.7}$ was 377 sfu at 1 AU and 390 sfu at the minimum Earth-Sun distance. These high values are usually associated with an active region rotating with the Sun; they could be elevated for a few days on either side of these peak values; and they could recur on the next solar rotation. These observations of the daily and 81-day mean $F_{10.7}$ radio flux were analyzed to estimate a likely 100-year value of 390 sfu for the daily mean and 280 sfu for the 81-day mean. No theoretical maximum benchmark is available, but a value of 500 sfu was used, with 390 sfu as the 81-day mean. These daily $F_{10.7}$ and 81-day mean values were used to drive the empirical NRLMSISE-00 neutral density model, and the values compared (as a percentage change) to reference values using 240 and 200 sfu for the daily and 81-day mean, respectively. Because events at these levels are clearly outside the parameters used to develop the empirical model, the estimates are likely to have large uncertainties. Physical models will be used in Phase 2 to support the estimates. Also in Phase 2, extreme-value methods will be explored for estimates of 1-in-100-year event likelihood.

⁴³ J. M. Picone et al., "NRLMSISE-00 Empirical Model of the Atmosphere: Statistical Comparisons and Scientific Issues," *Journal of Geophysical Research* 107 (2002): A12, 1468; J. T. Emmert, "Thermospheric Mass Density: A Review," *Advances in Space Research* 56 (2015): 773–824.

⁴⁴ B. R. Bowman et al., "A New Empirical Thermospheric Density Model JB2008 Using New Solar and Geomagnetic Indices," presentation at AIAA/AAS Astrodynamics Specialist Conference, 2008, AIAA 2008-6438.

⁴⁵ S. Bruinsma, "The DTM-2013 Thermosphere Model," *Journal of Space Weather and Space Climate* 5 (2015): A1.

⁴⁶ Space Weather Prediction Center, u.d. "F10.7 cm Radio Emissions." National Oceanic and Atmospheric Administration. <http://www.swpc.noaa.gov/phenomena/f107-cm-radio-emissions>

⁴⁷ Solar flux is measured in watts (W) per square meter (m^2) per hertz (Hz), with 1 sfu equal to $10^{-22} W m^{-2} Hz^{-1}$

Although not a direct consequence of atmospheric expansion, extended periods of enhanced EUV radiation will raise the fluence of atomic oxygen in LEO and degrade optics, organic films, advanced composites, and metallic surfaces.⁴⁸

Note that during solar radio bursts, the $F_{10.7}$ flux can be more than five orders of magnitude greater (see discussion in the section on benchmarks for solar radio bursts). During these times, the 10.7 solar radio flux no longer correlates with EUV and is no longer a suitable proxy.

Effects of Solar EUV Radiation Enhancement during Solar Flares on Upper Atmosphere Expansion

Solar flares are categorized by the power in the wavelength range of 0.1 to 0.8 nanometers (nm) in the X-ray part of the solar spectrum. The highest category of flare (X-class) has a power greater than 10^{-4} W m⁻². The largest solar flare on record is an X28 (2.8×10^{-3} W m⁻² in the 0.1 to 0.8 nm wavelength range), which was recorded by the GOES satellite on November 6, 2003, before the GOES instrument became overloaded. The ionospheric response at the time indicated the flare might have been closer to X45. The X-rays themselves have a small impact on neutral density because the energy is deposited deep within the atmosphere (~90–100 kilometers altitude). However, the EUV part of the solar spectrum can also increase during a flare, which does have a neutral density response, although the EUV flux is not always well correlated with the X-ray flux by which the flare is categorized. The Challenging Minisatellite Payload (CHAMP) satellite has recorded the neutral density response to numerous solar flares categorized as greater than X5.⁴⁹ The peak neutral density response was generally small, 5 to 10 percent at 400 kilometers altitude. On October 28, 2003 during an X17 flare, CHAMP recorded a peak density increase of 50 percent on the dayside of Earth for a few hours.⁵⁰

For the purposes of the neutral density response to the EUV part of the solar spectrum, the estimates for a 100-year flare is X30 and that for a theoretical maximum is X40.⁵¹ Palowsky and Ridley indicated that the density response at 400 kilometers altitude is linearly dependent on the total incident energy of the flare.⁵² The benchmark is established assuming a similar EUV spectrum and duration compared with the October 2003 event. The typical short duration of a flare of a few hours naturally constrains the temperature and density response, limiting the potential impact on satellite drag and orbit prediction. Therefore, the benchmark is restricted to the response at 400 kilometers at a median $F_{10.7}$ solar flux level of 150 sfu. In Phase 2, the need to expand the benchmark to the response at 250 and 850 kilometers altitude, and at extremely low ($F_{10.7} = 65$ sfu) and high ($F_{10.7} = 300$ sfu) solar activity, will be reassessed. Similar to daily EUV, since the thermospheric neutral winds do not increase substantially in response to a solar flare, the benchmark for this category is restricted to neutral density.

⁴⁸ A. C. Tribble et al., “Low Earth Orbit Thermal Control Coatings Exposure Flight Tests: A Comparison of U.S. and Russian Results,” NASA Contractor Report 4647, March 1995.

⁴⁹ H. Lühr et al., “Thermospheric Up-Welling in the Cusp Region: Evidence from CHAMP Observations.” *Geophysical Research Letters* 31 (2004): L06805.

⁵⁰ E. K. Sutton et al. “Neutral Density Response to the Solar Flares of October and November, 2003.” *Geophysical Research Letters* 33 (2006): L22101; B. T. Tsurutani et al., “The October 28 2003 Extreme EUV Flare and Resultant Extreme Ionosphere Effects: Comparison to Other Halloween Events and the Bastille Day Event,” *Geophysical Research Letters* 32 (2005): L03S09.

⁵¹ C. J. Schrijver et al. “Estimating the Frequency of Extremely Energetic Solar Events, Based on Solar, Stellar, Lunar, and Terrestrial Records.” *Journal of Geophysical Research* 117 (2012): A08103, based on an NRC study.

⁵² D. J. Pawlowski and A. J. Ridley, “The Effects of Different Solar Flare Characteristics on the Global Thermosphere,” *Journal of Atmospheric and Solar-Terrestrial Physics* 73 (2011): 1840–1848.

Effects of Coronal Mass Ejections Driving Geomagnetic Storms on Upper Atmosphere Expansion

Geomagnetic storms drive winds through ion drag and heat the thermosphere through auroral precipitation and Joule heating. Observations of neutral density and winds during large storms are available, and reasonable estimates of the response can be predicted using empirical models (e.g., NRLMSISE-00; DTM-2013; and JB2008) and simulated with physical models (e.g., the Coupled Thermosphere Ionosphere Plasmasphere Electrodynamics [CTIPe] model⁵³). Some of the largest storms in recent history stretch the limits of the empirical models, so estimates from the empirical models are likely to be uncertain by at least 50 percent for significant storms and nearly 100 percent for the largest storms. However, the empirical models, together with observations of large storms and guidance from the CTIPe physical model, can be used to extrapolate the response to more extreme events.

Although more likely to occur at the apex or descending phase of the solar cycle, large geomagnetic disturbances can theoretically occur during any level of background solar activity. In Phase 1, the neutral density and wind response to geomagnetic storms was estimated for mean solar activity ($F_{10.7} \sim 150$ sfu) for this benchmark. Since the relative response to storms depends on solar activity, the benchmark needs to be expanded in Phase 2 to quantify the response at very low ($F_{10.7} = 65$ sfu) and very high ($F_{10.7} = 300$ sfu) solar activity. The same storm drives a larger relative density at low solar activity, even though the absolute density is lower. Relative density and structure is particularly important for orbit prediction of debris and collision avoidance, which is a hazard at all levels of solar activity.

Estimates of the response to a 1-in-100-year geomagnetic storm are referenced to predictions of the solar wind condition of the important drivers, for example, the interplanetary magnetic field (IMF) magnitude and direction (particularly the magnitude of southward Bz),⁵⁴ and solar wind velocity and density. Two events are often cited in the literature characterizing an extreme event: the Carrington storm of 1859 and an event observed by NASA's Solar Terrestrial Relations Observatory Ahead (STEREO-A) spacecraft in July 2012.⁵⁵ For the Carrington event, Li et al.⁵⁶ estimate Bz to be in a southward direction between 60 to 70 nanotesla (nT), together with a solar wind speed exceeding 2,000 kilometers/second, and solar wind density exceeding $\sim 60 \text{ cm}^{-3}$. The magnetic storm disturbance index, Dst,⁵⁷ was predicted to be less than -1500 nT, although Siscoe, Crooker, and Clauer⁵⁸ suggested a more modest value of -850 nT. Note that the lowest measured Dst on record was recorded in March 1989 of -589 nT, during an event when the Hydro-Quebec and the U.S. East Coast power grids were severely disrupted. Geomagnetic storms can also be driven by high-speed streams in the solar wind, but they tend to be smaller in magnitude than CME driven storms so are not addressed specifically in the Benchmark estimates.

⁵³ T. J. Fuller-Rowell et al., "Storm-Time Response of the Thermosphere-Ionosphere System," in *Aeronomy of the Earth's Atmosphere and Ionosphere*, IAGA Special Sopron Book Series, vol. 2, chap. 32, edited by M. A. Abdu, D. Pancheva, and A. Bhattacharyya (Springer 2011).

⁵⁴ Bz indicates the north-south direction of the IMF. Solar wind particles will more easily enter Earth's magnetosphere and develop into a geomagnetic storm with a southward Bz than with a northward Bz.

⁵⁵ D. N. Baker et al., "A Major Solar Eruptive Event in July 2012: Defining Extreme Space Weather Scenarios," *Space Weather* 11 (2013): 585–591.

⁵⁶ X. Li et al., "Modeling of 1–2 September 1859 Super Magnetic Storm," *Advanced Space Research* 38 (2006): 273–279.

⁵⁷ M. Sugiura, "Hourly Values of Equatorial Dst for the IGY." In *Annals of the International Geophysical Year*, Part 1: 9–45 (Pergamon Press, 1964).

⁵⁸ G. Siscoe, N. U. Crooker, and C. R. Clauer, "Dst of the Carrington Storm of 1859." *Advanced Space Research* 38 (2006): 173–179.

Empirical models of magnetospheric convection⁵⁹ estimate Joule heating of 14,000 GW globally, with a Bz of -60 nT, V_{sw} of 1,500, and solar wind density of 10 cm^{-3} . This Joule heating power has significant uncertainty and is expected to be reduced by magnetospheric saturation.⁶⁰ Magnetospheric model simulations of extreme solar wind conditions could potentially reduce this uncertainty. In addition to producing the large-scale and global increase in neutral density, geomagnetic storms are also expected to produce significant structure, particularly at high and mid-latitudes. Polar orbiting objects and those in eccentric orbits are likely to be particularly vulnerable to neutral density structure.

4. Benchmarks

Solar Extreme Ultraviolet and Far Ultraviolet Radiation

The upper atmosphere expansion benchmarks for the neutral density response to the EUV flux on timescales greater than one day are shown in Table 11. The neutral density response is defined at 250 kilometers, 400 kilometers, and 850 kilometers altitude as percent increases relative to empirical model reference values using 240 and 200 sfu for the $F_{10.7}$ daily and 81-day mean, respectively. The $F_{10.7}$ levels for the 100-Year Benchmark are not too far outside the parameter space used to develop the empirical model, so are likely to have uncertainties of around 30%, not that much greater than the uncertainties in neutral density at $F_{10.7}$ peak levels of ~300 sfu. On the other hand, the uncertainties for the neutral density increases for the theoretical maximum are well outside parameter space of the empirical neutral density models and therefore the uncertainty increases to about a factor of 2.

Table 11. Benchmarks for global mean neutral density response to solar EUV on > 1-day timescales

Altitude	100-Year Benchmark (percent increase in neutral density in response to a daily $F_{10.7}$ of 390 sfu ^a with an 81-day mean of 280 sfu)	Theoretical Maximum (percent increase in neutral density in response to a daily $F_{10.7}$ of 500 sfu with an 81-day mean of 390 sfu)
250 kilometers	50%	100%
400 kilometers	100%	160%
850 kilometers	200%	300%

^a One solar flux unit (sfu) = $10^{-22} \text{ W m}^{-2} \text{ Hz}^{-1}$

Effects of Solar EUV Radiation Enhancement during Solar Flares on Upper Atmosphere Expansion

The upper atmosphere expansion benchmarks for the neutral density response to the EUV flux during a solar flare are shown in Table 12. The benchmarks assume a similar EUV spectrum and duration compared with the October 2003 X-class flare. The values quoted are peak dayside neutral density increases relative to the background before the flare. The values are quoted at 400 kilometers altitude only and are the response at a median $F_{10.7}$ solar flux level of 150 sfu. The EUV flux during a flare is not always well correlated with the X-ray flux by which the flare is categorized so the neutral density enhancements are uncertain to a factor of 2.

⁵⁹ See, for example, D. R. Weimer, "Improved Ionospheric Electrodynamics Models and Application to Calculating Joule Heating Rates," *Journal of Geophysical Research* 110 (2005): A05306.

⁶⁰ J. Raeder and G. Lu. "Polar Cap Potential Saturation during Large Geomagnetic Storms," *Advanced Space Research* 36 (1804, 2005).

Table 12. Benchmarks for peak dayside neutral density response to solar EUV on flare timescales

Altitude	100-Year Benchmark (peak dayside percent increase in response to an X30 flare)	Theoretical Maximum (peak dayside percent increase in response to an X40 flare)
400 kilometers	75%	135%

Phase 2 analyses will evaluate if the benchmark needs to be expanded to other altitudes and levels of solar activity. Considerable variability and uncertainty in the magnitude and duration of the EUV part of the spectrum exists during a solar flare.⁶¹ Prudent estimates for uncertainty in the peak density change and flare duration are at least a factor of two.

Coronal Mass Ejections Driving Geomagnetic Storms

In Phase 1, the neutral density benchmark in response to a 1-in-100-year CME was estimated at 400 kilometers altitude and at median $F_{10.7}$ solar flux level of 150 sfu. This benchmark is defined for peak global mean values of neutral density, but the values could equally be applied to orbit average density along polar or equatorial trajectories. The benchmark magnitude is the percent increase referenced to the NRLMSISE-00 values using solar and geomagnetic indices for the large geomagnetic storms of October 2003 (Halloween storm) or of July 2000 (Bastille Day storm).

Using the predicted 1-in-100-year solar wind values to drive the Weimer⁶² empirical magnetospheric convection model with expected magnetospheric saturation,⁶³ the benchmark assumes a peak global Joule heating rate of 10,000 GW. This energy was used to scale the input to a physics-based thermosphere-ionosphere model for the geomagnetic storm of December 2006. It was assumed the storm has a similar duration of about 12-hours. In that simulation, the thermospheric temperature exceeded 4,000 K, and neutral density exceeded empirical model estimates of the response to a Bastille Day- or Halloween-like storm by a factor of five (Table 13).

Table 13. Benchmarks for global mean neutral density response to CME.

Altitude	100-Year Benchmark (percent increase in response above values experienced during Halloween or Bastille Day storms)	Theoretical Maximum (percent increase in response above values experienced during Halloween or Bastille Day storms)
400 kilometers	400%	Phase 2

Results from the physical model simulation were used to estimate peak neutral winds, which are expected to exceed 2,000 meters/second, modulating the benchmark in-track apparent density by about 50 percent. Cross-track winds of these magnitudes will also significantly impede debris orbit prediction.

⁶¹ T. N. Woods et al., "New Solar Extreme-Ultraviolet Irradiance Observations during Flares." *Astrophysical Journal* 739, no. 2 (2011): 59.

⁶² Weimer, "Improved Ionospheric Electrodynamics Models and Application to Calculating Joule Heating Rates," *Journal of Geophysical Research* 110 (2005): A05306.

⁶³ J. Raeder et al., "Global Simulation of Space Weather Effects of the Bastille Day Storm." *Solar Physics* 204 (2001): 325.

The following are some additional characteristics in the neutral density response expected to impact orbit prediction of satellites and debris:

- *Neutral composition* mixing during a geomagnetic storm, changing the O/N₂ ratio, is expected to modulate the neutral density response by ±50 percent.
- *Auroral heating* is expected to increase global neutral density by 20 to 30 percent.
- *Neutral density structure* is expected to be produced during a geomagnetic storm. A small-scale structure (< 100 kilometer scale size) has only a small impact on satellite drag due to the brief period of influence (~10 seconds) for typical satellite orbit velocities (~8 kilometers/second). Wave structure (peaks and troughs) at this resolution will also have only a small impact on satellite orbit since the net drag integrates through the peaks and troughs. A larger scale structure (~500 kilometers), such as associated with the cusp⁶⁴ or auroral oval, however, can have an impact on particular orbit trajectories and eccentric orbits. During an extreme event, a 500-kilometer structure and waves would be expected to deviate 50 to 100 percent from the background.⁶⁵

The uncertainties of the benchmark estimates for the neutral density response to an extreme CME are currently at least 100 percent, meaning the response could be up to twice the current estimates. It is also possible that the magnetosphere saturates, and the response to an extreme event would actually be no more than the response to some of the super-storms of the past (e.g., Halloween or Bastille Day storms). Extreme storms are likely to occur at the same time as elevated EUV flux, so the effects could be additive. In these circumstances, the cumulative effect could increase density above previously observed storms by a factor of ten. Finally, extreme storms are likely to occur at the same time as elevated EUV flux so the effects could be additive. In these circumstances the cumulative effect could increase density above previously observed storms by a factor of ten.

A significant uncertainty in the geomagnetic storm simulation is the cooling rates in the model, which were calculated based on an extrapolation of the Marsh, Solomon, and Reynolds SNOE NO empirical model (NOEM).⁶⁶ The cooling rates in CTIpe come firstly from vertical heat conduction from the upper to lower thermosphere, and then from infrared radiative cooling, primarily from the 5.3- μ m nitric oxide (NO) band. NO cooling has been referred to as a “thermostat” for the system by Mlynczak et al.⁶⁷ Auroral precipitation, as well as serving as a source of heat and ionization during a geomagnetic storm, also produces NO and increases the cooling rate. Since the Marsh NOEM code has to be extrapolated from lower geomagnetic storm levels to these more extreme conditions, inevitably the cooling rate estimates have significant uncertainty. In addition, Knipp et al. have reported that the NO production during a storm can persist into the recovery and drive an “overcooling” and collapse of the thermosphere, leading to significant drag reduction.⁶⁸

⁶⁴ H. Lühr et al., “Thermospheric Up-Welling in the Cusp Region: Evidence from CHAMP Observations,” *Geophysical Research Letters* 31 (2004): L06805.

⁶⁵ R. L. Anderson, G. H. Born, and J. M. Forbes, “Sensitivity of Orbit Predictions to Density Variability,” *Journal of Spacecraft and Rockets* 46, no. 6 (2009).

⁶⁶ D. R. Marsh, S. C. Solomon, and A. E. Reynolds, Empirical Model of Nitric Oxide in the Lower Thermosphere,” *Journal of Geophysical Research* 109 (2004): A07301, doi:10.1029/2003JA010199

⁶⁷ M. Mlynczak et al. “The Natural Thermostat of Nitric Oxide Emission at 5.3 μ m in the Thermosphere Observed During the Solar Storms of April 2002,” *Geophysical Research Letters*, 30, no. 21 (2003), doi:10.1029/2003GL017693

⁶⁸ D. J., Knipp et al., “Data and Model Views of Energy Input to the Dayside Thermosphere, When the East-West Interplanetary Magnetic Field Is Large,” presented at AGU Fall Meeting, San Francisco, California, 2011.

Bibliography

This bibliography contains supplemental references that provide important background to the topics discussed in the SPACE WEATHER EMP BENCHMARKS.

Akmaev, R., and V. Fomichev. "Cooling of the Mesosphere and Lower Thermosphere Due to Doubling of CO₂." *Annales Geophysicae* 16 (1998): 1501–1512.

Bostanjyan, N. Kh., A. A. Chilingarian, V. S. Eganov, and G. G. Karapetyan. "On the Production of Highest Energy Solar Protons at 20 January 2005." *Advanced Space Research* 39 (2007): 1454–1457. doi:10.1016/j.asr.2007.03.024

Bowman, B. R. "True Satellite Ballistic Coefficient Determination for HASDM." in AIAA/AAS Astrodynamics Specialist Conference and Exhibit, 5–8 August 2002. Monterey, California. AIAA 2002–4887.

Cannon, P., M. Angling, L. Barclay, and S. Bruinsma. "The DTM-2013 Thermosphere Model." *Journal of Space Weather Space Climate* 5 (2015): A1. doi:10.1051/swsc/2015001

Cannon, P. S., "Extreme Space Weather—A Report Published by the UK Royal Academy of Engineering." *Space Weather* 11 (2013). doi:10.1002/swe.20032

Cliver, E. W., and W. F. Dietrich. "The 1859 Space Weather Event Revisited: Limits of Extreme Activity." *Journal of Space Weather Space Climate* 3 (2013): A31. doi:10.1051/swsc/2013053

Copeland, K., "CARI-7A: Development and Validation" *Radiation Protection Dosimetry*. 2017. doi:10.1093/rpd/ncw369

Dryer, M. "The August 1972 Events," *Space Science Reviews* 19, no. 4/5 (1976):409–410.

Dryer, M., Z. Smith, C. D. Fry, W. Sun, C. S. Deehr, and S.-I. Akasofu. "Real-time Shock Arrival Predictions During the 'Halloween 2003 Epoch.'" *Space Weather* 2, no. 9 (September 2004). doi:10.1029/2004SW000087

Falconer, D., A. F. Barghouty, I. Khazanov, and R. Moore. 2011. "A Tool for Empirical Forecasting of Major Flares, Coronal Mass Ejections, and Solar Particle Events from a Proxy of Active-Region Free Magnetic Energy." *Space Weather* 9, no. 4 (April 2011). doi:10.1029/2009SW000537

Fennell, J. F., J. L. Roeder, and H. C. Koons. "Substorms and Magnetic Storms from the Satellite Charging Perspective." In Ling-Hsiao Lyu, Editor, *COSPAR Colloquia Series 12* (2002): 163–173. doi:10.1016/S0964-2749(02)80215-3

Fennell, J. F., H. C. Koons, M. W. Chen, and J. B. Blake. "Internal Charging: A Preliminary Environmental Specification for Satellites." *IEEE Transactions on Plasma Science* 28, no. 6 (December 2000): 2029–36. doi:10.1109/27.902230

Hudson, M. K., B. T. Kress, J. E. Mazur, K. L. Perry, and P. L. Slocum. "3D Modeling of Shock-Induced Trapping of Solar Energetic Particles in the Earth's Magnetosphere." *Journal of Atmospheric and Solar-Terrestrial Physics* 66 (2004): 1389–1397. doi:10.1016/j.jastp.2004.03.024

Implementation of MAGNETOCOSMICS Geant4 in the SPENVIS Environment,
<https://www.spennis.oma.be/help.php>

ISO 14222. 2013. "Space Environment (Natural and Artificial)—Earth Upper Atmosphere." International Standards Organization, Geneva, Switzerland.

- Lanzerotti, L. J., and C. G. Maclennan. "Solar Particle Observations during the August 1972 Event, in: Correlated Interplanetary and Magnetospheric Observations;" Proceedings of the Seventh ESLAB Symposium, Saulgau, West Germany, May 22–25, 1973. (A75-19126 06-46) Dordrecht, D. Reidel Publishing Co., 1974, 587–596.
- Laurenza, M., E. W. Cliver, J. Hewitt, M. Storini, A. Ling, C. C. Balch, and M. L. Kaiser. "A Technique for Short-Term Warning of Solar Energetic Particle Events based on Flare Location, Flare Size, and Evidence of Particle Escape." *Space Weather* 7, no. 4 (April 2009). doi:10.1029/2007SW000379
- Li, X., R. S. Selesnick, D. N. Baker, A. N. Jaynes, S. G. Kanekal, Q. Schiller, L. Blum, et al. "Upper Limit on the Inner Radiation Belt MeV Electron Intensity." *Journal of Geophysical Research* 120, no. 2 (February 2015): 1215–28. doi:10.1002/2014JA020777
- Lingenfelter, R. E., and H. S. Hudson. "Solar Particle Fluxes and the Ancient Sun." In *The Ancient Sun: Fossil Record in the Earth, Moon and Meteorites*. Proceedings of the Conference, Colorado, October 16–19, 1979, 69–79. Edited by R. O. Pepin, J. A. Eddy, and R. B. Merrill. Oxford: Pergamon Press, 1980.
- Matthiä, D., B. Heber, G. Reitz, M. Meier, L. Sihver, T. Berger, and K. Herbst. "Temporal and Spatial Evolution of the Solar Energetic Particle Event on 20 January 2005 and Resulting Radiation Doses in Aviation." *Journal of Geophysical Research* 114 (2009): A08104. doi:10.1029/2009JA014125
- Meredith, N. P., R. B. Horne, J. D. Isles, K. A. Ryden, A. D. P. Hands, and D. Heynderickx. "Extreme Internal Charging Currents in Medium Earth Orbit: Analysis of SURF Plate Currents on Giove-A." *Space Weather* 14 (2016): 578–591. doi:10.1002/2016SW001404
- Meredith, N. P., R. B. Horne, J. D. Isles, and J. C. Green. "Extreme Energetic Electron Fluxes in Low Earth Orbit: Analysis of POES E > 30, E > 100, and E > 300 keV Electrons." *Space Weather* 14 (2016) doi:10.1002/2015SW001348
- Mewaldt, R. A., A. J. Davis, K. A. Lave, R. A. Leske, E. C. Stone, M. E. Wiedenbeck, W. R. Binns, E. R. Christian, A. C. Cummings, G. A. de Nolfo, M. H. Israel, A. W. Labrador, and T. T. von Roseninge. "Record-Setting Cosmic-Ray Intensities in 2009 and 2010." *Astrophysical Journal Letters* 723, no. 1 (October 2010): L1–L6. doi:10.1088/2041-8205/723/1/L1
- Miyake, F., K. Masuda, T. Nakamura. "Another Rapid Event in the Carbon-14 Content of Tree Rings." *Nature Communications* 4 (2013): 1748.
- National Research Council (NRC). *Limiting Future Collision Risk to Spacecraft: An Assessment of NASA's Meteoroid and Orbital Debris Programs*. Washington, D.C.: National Academies Press. 2011.
- Núñez, M. 2011. "Predicting Solar Energetic Proton Events (E > 10 MeV)." *Space Weather* 9, no. 7 (July 2011). doi:10.1029/2010SW000640
- Núñez, M. 2015. "Real-Time Prediction of the Occurrence and Intensity of the First Hours of >100 MeV Solar Energetic Proton Events." *Space Weather* 13, no. 11 (November 2015): 807–819. doi:10.1002/2015SW001256
- Posner, A. 2007. "Up to 1-Hour Forecasting of Radiation Hazards from Solar Energetic Ion Events with Relativistic Electrons." *Space Weather* 5, no. 5 (May 2007). doi:10.1029/2006SW000268
- Posner, A., B. Heber, O. Rother, and S. Guetersloh 2007. "A New Trend in Forecasting Solar Radiation Hazards," *Space Weather* 7, no. 5 (May 2007), S05001.

- Posner, A., N. A. Schwadron, D. J. McComas, E. C. Roelof, and A. B. Galvin. 2004. "Suprathermal Ions Ahead of Interplanetary Shocks: New Observations and Critical Instrumentation Required for Future Space Weather Monitoring." *Space Weather* 2, no. 10 (October 2004). doi:10.1029/2004SW000079
- Reedy, R. C. 1997. "Radiation Threats from Huge Solar Particle Events." NASA Conference Publication 3353. Presentation at Conference on the High Energy Radiation Background in Space. Snowmass, Colorado, July 22–23, 1997. Edited by P. H. Solomon, 77–79.
- Scarpulla, J., and A. Yarbrough. "What Could Go Wrong? The Effects of Ionizing Radiation on Space Electronics." *Crosslink* 4 (2003): 15–19, and references therein.
- Smith, Z., and R. Zwickl. 1999. "Forecasting Geomagnetic Storms Using Energetic Particle Enhancements." In *Solar Wind Nine: Proceedings of the Ninth International Solar Wind Conference*. Edited by S. Habbal et al., 577. Nantucket, Massachusetts, October 5–9, 1998: Woodbury, N. Y.: American Institute of Physics, 1999.
- Storz, M. F., B. R. Bowman, M. J. I. Branson, S. J. Casali, W. K. Tobiska. "High Accuracy Satellite Drag Model (HASDM)." *Advanced Space Research* 36 (2005): 2497–2505.
- Thomsen, M. F., M. H. Denton, B. Lavraud, and M. Bodeau. "Statistics of Plasma Fluxes at Geosynchronous Orbit over More than a Full Solar Cycle." *Space Weather* 5 (2007): S03004. doi:10.1029/2006SW000257
- Tsurutani, B. T., and G. S. Lakhina. "An Extreme Coronal Mass Ejection and Consequences for the Magnetosphere and Earth." *Geophysical Research Letters* 41 (2014): 287–292. doi:10.1002/2013GL058825
- Welling, D. T., "The Long-Term Effects of Space Weather on Satellite Operations." *Annales Geophysicae* 28 (2010): 1361–1367.
- Wilson, J. W., F. A. Cucinotta, J. L. Shinn, L. C. Simonsen, R. R. Dubbed, W. R. Jordan, T. D. Jones, et al. "Shielding from Solar Particle Event Exposures in Deep Space." *Radiation Measurements* 30, no. 3 (June 1999): 361–82. doi:10.1016/S1350-4487(99)00063-3
- Xapsos, M. A., C. Stauffer, T. Jordan, J. L. Barth, and R. A. Mewaldt. "Model for Cumulative Solar Heavy Ion Energy and Linear Energy Transfer Spectra." *IEEE Transactions on Nuclear Science* 54, no. 6 (December 2007): 1985–9. doi:10.1109/TNS.2007.910850

Abbreviations

ACE	Advanced Composition Explorer
ACR	anomalous cosmic ray
AU	astronomical unit
C	carbon
CHAMP	Challenging Minisatellite Payload
cm	Centimeter
CME	coronal mass ejection
CO ₂	carbon dioxide
CTIPe	Coupled Thermosphere Ionosphere Plasmasphere Electrodynamics
DHS	Department of Homeland Security
DOC	Department of Commerce
DOD	Department of Defense
DOE	Department of Energy
DOI	Department of the Interior
DOT	Department of Transportation
DSCOVR	Deep Space Climate Observatory
Dst	Disturbance storm time index
EUV	extreme ultraviolet
eV	electron volt
EVT	extreme value theory.
F _{10.7}	10.7-centimeter solar radio flux
FCC	Federal Communications Commission
Fe	iron
FUV	far ultraviolet
GCR	galactic cosmic ray
GEO	geostationary Earth orbit
GeV	gigaelectron volt
GHz	gigahertz
GLE	ground-level event
GNSS	Global Navigation Satellite System
GOES	Geostationary Operational Environmental Satellite
GPS	Global Positioning System

HAF	highest affected frequency
H	hydrogen
He	helium
HEO	highly elliptical orbit
HF	high frequency
hmF ₂	height of the F ₂ layer
IEEE	Institute of Electrical and Electronics Engineers
IMF	Interplanetary Magnetic Field
keV	kiloelectron volts
kHz	kilohertz
km	kilometer
LANL	Los Alamos National Laboratory
LEO	low Earth orbit
LIS	local interstellar spectra
MEO	medium Earth orbit
MeV	megaelectron volts
MHz	megahertz
MIT	magnetosphere-ionosphere-thermosphere
MUF	maximum usable frequency
MV	megavolt
N ₂	molecular nitrogen
NASA	National Aeronautics and Space Administration
NERC	North American Electric Reliability Corporation
NmF ₂	peak density of the F ₂ Layer
NOAA	National Oceanic and Atmospheric Administration
NSF	National Science Foundation
NSTC	National Science and Technology Council
nT	nanotesla
NTIA	National Telecommunications and Information Administration
O	oxygen
OSTP	Office of Science and Technology Policy
R&D	research and development
R _E	radius of Earth

RSTN	Radio Solar Telescope Network
SEP	solar energetic particle
sfu	solar flux unit
SIS	Solar Isotope Spectrometer
SPENVIS	Space Environment Information System
STEM	Science, Technology, Engineering, and Mathematics
TEC	Total Electron Content
U.S.C.	United States Code
UHF	Ultra High Frequency
VHF	very high frequency
V/km	volt(s) per kilometer